BILINGUAL
PUBLISHING CO.
Pioneer of Global Academics Since 1984

2019 April

Journal of Metallic Material Research

01.

April Volume 2 Issue 1 ISSN 2630-5135 (Online)

BILINGUAL
PUBLISHING CO.
Pioneer of Global Academics Since 1984

Editor-in-Chief

Dr. Oleg Valentinovich
Sobol, Ukraine

Editorial Board Members

Shuo Chen, United States
Changrui Wang, China
Recep Karadag, Turkey
Madhukar Eknath Navgire, India
Unal Camdali, Turkey
Jitendra Kumar Singh, Korea
Abhay Nanda Srivastva, India
Vivek Patel, India
Aybaba Hançerlİoğullari, Turkey
Bandar Abdulaziz AlMangour, Saudi Arabia
Soumen Maiti, India
Jonathan David Parker, Canada
Jingyuan Yan, United States
Satyanarayana Sirasani, India
Xiaoan Hu, China
Derya Dispinar, Turkey
Samson jerold samuel Chelladurai, India
Akash Deep Sharma, India
Dan Dobrotă, Romania
Asit Kumar Gain, Australia
Dragica Milan Minic, Serbia
Zabiollah Mahdavifar, Iran
Chandan Pandey, India
Mahnaz Mahdavi Shahri, Iran
Janarthanan Gopalakrishnan, India
Deniz Uçar, Turkey
Weidong Song, China
Attoui Aissa, Algeria
Mohammad Farnush, Iran
Qiaoli Lin, China
Hajar Zarei Se Dehi Zadeh, Iran
Subravel Visvalingam, India
Asaminew Abiyu Cherinet, Ethiopia
Arif Gök, Turkey
Ning Li, China
Fufa Wu, China
Wenchun Jiang, China
Saeed Zeinali Heris, Iran
Himadri Bhusan Sahoo, India
Vladimir Victorovich Lukov, Russian Federation
Abhishek Ghosh, India
KangHua Chen, China
Pradeep L Menezes, United States
Shuhua Zhang, China
Naushad Ahmad, India
S Selvam, India
Guocheng Zhu, China
Mohamed Kamal ElFawkhry, India
Mohammad Hassan Shirani Bidabadi, China
Mohd Azli Salim, Malaysia
Vladimir Mikhailov Yegorovich, Russian Federation
Kaveh Sheikhi Moghaddam, Iran
Robin Gupta, India
Sergey Vasilevich Byvaltsev, Russian Federation
Nitin Saini, India
Ramesh Balakrishnan, India

Alexander Evgenievich Barmin, Ukraine
Khitam Abdulhussein Saeed, Malaysia
Sertan Ozan, Turkey
Anand Krishnan, South Africa
Farshad Darab-Golestan, Iran
Mohammadreza Elahifard, Iran
Paparao Mondi, India
Zbigniew Ranachowski, Poland
Sami ullah Rather, Saudi Arabia
Nickolaj Nikolayevich Rulyov, Ukraine
Oğuzhan Keleştemur, Turkey
Shengqiang Ma, China
Md Saiful Islam, Bangladesh
Ajay Kumar Choubey, India
Saeed Kakaei, Iran
Hojat Jafari, Iran
Yuhan Liang, United States
Ahmed Wagih, Egypt
Bhanodaya Kiran Babu Nadikudi, India
Rong Liu, Canada
Mahmoud Pakshir, Iran
Changhai Zhou, China
Vishal Ishvarbhai Lad, United States
Hossein Ghasemi Mobtaker, Iran
Francesco Caridi, Italy
Konstanti Viktorovich Ivanov, Russian Federation
Dipak Kumar, India
Americo Scotti, Brazil
Ziad Salem Abu-Hamatteh, Jordan
Mohsen Vafaeifard, Malaysia
Hülya - Demirören, Turkey
Tahir Mohiuddin Bhat, India
Hamit Özkan Gülsoy, Turkey
Sandhya Dwevedi, India
Sergey Nikolaevich Lezhnev, Kazakhstan
Faysal Fayez Eliyan, Canada
Shouxun Ji, United Kingdom
Patrice Berthod, France
Moslem Mansour Lakouraj, Iran
Akhyar - Akhyar, Indonesia
Chih-Chun Hsieh, Taiwan
Recep Sadeler, Turkey
Lutfiddin Omanivich Olimov, Uzbekistan
Mahmoud Ebrahimi, Iran
Lineker Max Goulart Coelho, Brazil
Aslıhan Katip, Turkey
Serkan ISlak, Turkey
Murat Sarıkaya, Turkey
Yaofeng Chang, United States
Mehmet Kaya, Turkey
Yahya Absalan, Russian Federation
Xiang Wang, China
Meilinda Nurbanasari, Indonesia
Rizk Mostafa Shalaby, Egypt
Anatolii Michailovich Lepikhin, Russian Federation

Volume 2 Issue 1 • April 2019 • ISSN 2630-5135 (Online)

Journal of
Metallic Material
Research

Editor-in-Chief

Dr. Oleg Valentinovich

BILINGUAL
PUBLISHING CO.
Pioneer of Global Academics Since 1984

Volume 2 | Issue 1 | April 2019 | Page 1-38
Journal of Metallic Material Research

Contents

Article

Review

Copyright

BILINGUAL PUBLISHING CO.
Pioneer of Global Academics Since 1984

Journal of Metallic Material Research
https://ojs.bilpublishing.com/index.php/jmmr

REVIEW

Preparation and Properties of Graphene-based Inorganic Nanocomposites

Qing Liao[1] **Tingting Song**[2*]

1. Hezhou University, Hezhou, Guangxi, 542899, China
2. China West Normal University, Nanchong, Sichuan, 637002, China

ARTICLE INFO

Article history
Received: 5 April 2019
Accepted: 6 April 2019
Published Online: 19 April 2019

Keywords:
Graphene-based inorganic nanocomposites
Preparation
Properties

ABSTRACT

Graphene is a two-dimensional hexagonal monoatomic layer crystal composed of carbon atoms, which exhibits the shape of a honeycomb and plays an important role in the fields of optics and mechanics. It also has the advantages of high specific surface area, strong chemical stability and special planar structure. It is an ideal carrier for carrying various inorganic compounds and is suitable for the development of high performance graphene-based inorganic nanocomposites.[1] Based on this, the paper introduces the characteristics of graphene, expounds the related content of graphene-based inorganic nanocomposites, and studies the preparation methods and properties of graphene-based inorganic nanocomposites.

1. Introduction

At this stage, graphene has been applied to the development of various fields such as chemistry, physics, and materials science. It mainly uses a single layer of atomic thick graphene nanosheets as a support surface to anchor functional nanomaterials. Graphene and functional nanomaterials together constitute a new type of nanocomposites, which have been applied in the fields of catalysis and optoelectronics. Through related research, it has been found that graphene and various inorganic nanomaterials are fused into a composite material, which not only ensures the characteristics of graphene and inorganic nanomaterials, but also has new characteristics, and has been applied in various devices.

2. The Properties of Graphene

2.1 Mechanical Property

The structure of graphene material has certain special characteristics, and it has many special properties. In general, the carbon atoms constituting the graphene are arranged according to a regular hexagon to form a honeycomb structure. In the case where an external force is applied to the graphene, the surface of the carbon atom is deformed, and it is possible to adapt to the external force without rearranging it, thereby ensuring the stability of the graphene structure, so that the graphene exhibits strong mechanical properties. At this stage, the graphene material is the strongest in the known materials, its tensile strength is 125GPa, the elastic modulus is 1.1TPa, and the graphene strength is about 100 times that of the con-

---

**Corresponding Author:*
Tingting Song,
China West Normal University, No. 1 Shida Road, Shunqing District, Nanchong, Sichuan, 637002, China;
E-mail: songttphy@gmail.com

DOI: https://doi.org/10.30564/jmmr.v2i1.802

ventional one.[2] In addition, graphene film has both tough properties and strong flexibility. The main performance is that graphene can be bent and folded in any direction to ensure that the crystal structure does not change.

2.2 Electrical Property

Graphene materials have a strong charge transport capability, and their transport process satisfies the description of mass-free relativistic particles. Graphene is a zero-gap two-dimensional semi-metal material with a valence band and partial overlapping of electronic bands. At room temperature, the charge transport process in graphene exhibits an unconstrained parabolic electronic splitting relationship. In addition, graphene also has a strong bipolar electric field effect. In the case of a high carrier concentration, it is necessary to apply a normal voltage, and the electron mobility in the room temperature will reach $10000cm^2V^{-1}s^{-1}$, and the graphene suspension has a low-temperature electron mobility close to $20000cm^2V^{-1}s^{-1}$ at a carrier concentration of $5\times10^9cm^{-2}$, which is a very rare type of semiconductor material.

2.3 Optical Property

The optical properties of graphene have certain uniqueness. The light transmittance of the single-layer graphene is 97.7% or more, but the light transmittance has no relationship with the incident light wavelength, and exhibits a linear relationship with the number of layers of graphene. At the same time, graphene itself has nonlinear saturable absorption characteristics, which has been applied in the field of laser mode-locking technology. It mainly outputs laser light by laser pulse width under the action of graphene compression, which makes the saturable absorber prepared by graphene favorable for full-band mode-locking, and the optical properties of graphene itself have been applied in the field of ultrafast photonics.[3]

2.4 Thermal Property

At room temperature, the thermal conductivity of the single-layer graphene dispersion is relatively high, about $5000Wm^{-1}K^{-1}$, and the thermal conductivity of the single-layer graphene in the silicon base is lower than that of the graphene dispersion, which is about $600Wm^{-1}K^{-1}$. However, the thermal conductivity of graphene in the silicon base is continuously reduced, mainly because the interface diffusibility of the silicon-based graphene is relatively strong, resulting in the loss of phonons. Therefore, the thermal conductivity of graphene is 2 times and 50 times higher than that of copper and silicon.

3. Related Content Analysis of Graphene-based Inorganic Nanocomposites

Graphene nanocomposites are materials formed by dispersing metal nanoparticles in graphene sheets. At this stage, the focus of researchers on the study of graphene nanocomposites is the application of functional nanoparticles of silicon metal to modify graphene. In this way, composite materials with better properties than metals can be obtained, the application value is relatively high, the consumption of silicon metal can be reduced, and the economic value is relatively high. At the same time, graphene is a two-dimensional carbon nanomaterial, which provides more space for modifying various materials, making graphene fully contact with related materials.[4] In addition, Graphene has high chemical stability, optical and mechanical properties, and relatively low production cost. It is suitable for the development of high-performance composite materials. The effective integration of graphene and inorganic nanomaterials will become an important development trend in the future. In the development of modern society, many inorganic nanoparticles, such as metal materials, semiconductor materials, topological insulator materials and graphene, are effectively integrated, which constitutes a graphene-based inorganic nanocomposite material, which has special electrical properties, optical properties and catalytic properties, and has been widely used in the fields of biosensing, catalysis, optoelectronics, electrochemistry, and sewage treatment.

4. The Preparation of Graphene-based Inorganic Nanocomposites

4.1 Chemical Reduction Method

The chemical reduction method is a common method for preparing graphene-based inorganic nanocomposites, which mainly comprises graphene and metal into a graphene oxide solution and a metal salt solution, on the basis of the fusion of the two, a reducing agent is added, and a graphene-based inorganic nanocomposite is prepared by a redox method. There are many types of metal oxides, and many different metals are effectively reduced on the basis of the chemical reduction method. For example, related scholars have applied a two-step chemical reduction method to prepare graphene/Ag nanocomposites.

4.2 Thermal Evaporation Method

The thermal evaporation method is also a commonly used method for preparing graphene-based inorganic nanocomposites. The main feature of this method is that it is

DOI: https://doi.org/10.30564/jmmr.v2i1.802

easy to operate, efficient, and does not require a lot of cost. It is mainly based on the heating material, so that the evaporation vaporization is deposited into the substrate. For example, a person skilled in the art can apply a thermal evaporation method to deposit Au nanoparticles on a graphene surface. In the case where Au deposited in the n-layer graphene acts on the base, the surface properties of the graphene may be different, resulting in Au in the thickness-dependent state of the n-layer grapheme, which effectively identifies high-throughput, high spatial resolution graphene.

4.3 Electrochemical Deposition Method

The electrochemical deposition method has high preparation efficiency. This method can directly deposit metal nanomaterials in the graphene matrix, which is environmentally friendly and highly efficient. Relevant personnel can use the electrochemical deposition method to dissolve the graphene sheet into the plating solution, and add a surfactant to form a Ni/graphene composite after stirring. When the amount of graphene material added is 0.05g/L, the elastic modulus of the Ni/graphene composite material reaches 240GPa and the hardness reaches 4.6GPa, which greatly enhances the strength of the material.[5]

5. The Applications of Graphene and Its Composites

5.1 The Application in Photoelectric Field

Graphene has the characteristics of large specific surface area and high electrical conductivity. Graphene-based nanocomposites will become ideal materials for supercapacitors. Graphene's large π-electron system is suitable for the fabrication of nonlinear optical materials with excellent performance, and will be widely used in image processing, optical switching, optical storage and other fields. At the same time, graphene materials also have great application advantages in solar cells. They mainly apply graphene oxide on the surface of quartz. After thermal reduction treatment, the transmittance in the range of 400 to 1800 nm is about 80%, therefore, graphene-based nanocomposites will replace traditional silicon conductive materials and exert great advantages.[6]

5.2 The Application in Biomedical Field

Graphene material has the characteristics of large specific surface area and good biocompatibility. It is an ideal drug carrier and will be widely used in the field of biomedicine. For example, using soluble graphene as a drug carrier, the application of hydrogen bonding is beneficial to ensure the efficient loading of the antitumor drug doxorubicin in graphene; nanographene has strong antibacterial properties, and its inhibition rate against Escherichia coli is over 90%, which will not cause toxicity to mammalian cells.

5.3 The Application in Catalytic and Energy Storage Materials

In the development of modern society, many carbon materials, such as graphite, activated carbon, carbon nanotubes, etc., are the main carriers of the catalyst. Related studies have shown that the structure of the carbon support is directly related to the basic properties of the supported catalyst. Graphene has a regular two-dimensional surface structure and is an ideal template-supporting catalyst. The composite obtained by the combination of Pd nanoparticles and graphene oxide has high catalytic activity. Moreover, the related art has designed a novel 3D carbon material with adjustable pore size, which is called a graphene column, which is fused with lithium atoms and has a hydrogen storage capacity of 611wt%. Therefore, graphene hydrogen storage materials will be widely used in the field of energy storage.

5.4 The Application in DNA Detection

DNA is the basic unit that constitutes the biological function of the organism and maintains the normal functioning of various functions of the organism. The structural changes, deletions and errors will change the genetic information and trigger a series of diseases. In the development of modern society, researchers are committed to the research of DNA separation and detection technology, which will become the focus of medical diagnosis, drug development and bioengineering. Especially in the process of disease prevention, diagnosis and treatment, relevant personnel are paying more and more attention to DNA base sequence analysis and base mutation detection. Related studies have found that DNA detection methods are mainly electrochemical methods, electrochemiluminescence and fluorescence methods. Due to the relatively strong photoelectric properties of graphene, researchers have begun to study the application of graphene in the field of DNA analysis. Related technical personnel fuse DNA strands and composites, and follow the principle of base-complementary matching and complementary DNA strands to form a double-helical structure. The quenching principle of graphene fluorescence by DNA strands is used to measure the change of graphene fluorescence performance before and after binding to complementary strands, which measures complementary DNA strands, opening the application of graphene in the field of DNA detection.[7]

DOI: https://doi.org/10.30564/jmmr.v2i1.802

6. The Prospects for the Development of Graphene Materials

In the development of modern society, researchers are paying more and more attention to the study of graphene and its composite materials. By using different methods to prepare high-quality, large-area graphene materials, on the basis of optimizing and perfecting the graphene preparation process, the preparation of graphene materials is reduced, and it is applied to the development of various fields. Graphene materials have certain uniqueness. From the production point of view, graphite is the raw material for the production of graphene, which has many raw materials and low prices. Therefore, many countries have established graphene technology research and development centers, and tried to apply them to the development of industry, technology, electronics and other fields. For example, the European Commission has set up a special research and development program for graphene as a "New Future Flagship Technology Project".

In addition, in the future development, graphene materials will be used in more fields, which require researchers to increase the research of graphene preparation process. At this stage, more and more methods for the preparation of graphene will be widely applied to the development of various fields. However, graphene industrialization research is still in the initial stage of development, and the application of many fields cannot reflect the performance of graphene. Many researchers in the world are exploring the application of "killer level". In the future, there are too many challenges in testing and certification. It is necessary to continuously innovate in means and methods to give full play to the function of graphene materials.[8]

7. Conclusion

In summary, graphene material structure has certain peculiarity, its electrical properties, physical properties, thermal properties are relatively good, and the preparation of graphene is rich in raw materials, low cost, suitable for optoelectronics, multi-phase reminder, biomedicine and other fields. In the development of the new era, the society has paid more and more attention to the research of graphene composite materials, but there are still a series of problems. Relevant personnel need to actively solve the problem of large-scale preparation of graphene and development of graphene composites to ensure the application of graphene is more extensive.

References

[1] Ming Zhang, Fengqi Zhao, Yanjing Yang, Wengang Qu, Na Li, Jiankan Zhang. Research progress on the influence of graphene-based materials on the properties of energetic materials[J]. Chinese Journal of Energetic Materials, 2018, 26(12):1074- 1082. (in Chinese)

[2] Yurun Zeng, Xiaoxia Li, Yuxiang Guo, Deyue Ma. Research progress in preparation and application of graphene-based ternary composites[J]. Modern Chemical Industry, 2018, 38(10):43-47. (in Chinese)

[3] Mengyu Qi, Shuhui Li, Yuzhi Du, Peng Ye, Heliang Han, Qing He, Meng Wang. Research Progress of Graphene-based Nanocomposites[J]. Functional Materials Information, 2017, 14(03):10-18. (in Chinese)

[4] Mengyu Qi, Shuhui Li, Yuzhi Du, Peng Ye, Heliang Han, Qing He, Meng Wang. Research Progress of Graphene-based Nanocomposites[J]. Journal of Functional Materials, 2017, 48(03):3042-3049. (in Chinese)

[5] Xuecheng Zhan, Xin Zou, Haowen Ma, Bin Wang, Xiaoli Hu, Limin Sun, Yundi Zheng. Research progress of graphene-based catalysts and their catalytic hydrogenation applications[J].Petrochemical Technology & Application, 2017, 35(02): 160-164. (in Chinese)

[6] Bo Zhao, Li Jiang, Minghui Yuan, Xianzhu Fu, Rong Sun, Zhengping Wang. Preparation of graphene and its composites by electrochemical method[J]. Journal of Electrochemistry, 2016, 22(01):1-19. (in Chinese)

[7] Changnan Li, Pei Chen, Yinan Sun, Yuyu Dong, Yajie Guo, Guangjian Wang. Research Progress in Preparation and Application of Graphene-Based Materials[J]. Journal of Huaibei Normal University (Natural Sciences), 2015, 36(03):53-62. (in Chinese)

[8] Jiahua Zhang, Yaming Wang, Shuisheng Wu, Lihong Jiang. Progress in catalytic application of graphene-based composites[J]. Journal of Functional Materials, 2015, 46(16):16016-16022. (in Chinese)

DOI: https://doi.org/10.30564/jmmr.v2i1.802

BILINGUAL PUBLISHING CO.
Pioneer of Global Academics Since 1984

Journal of Metallic Material Research
https://ojs.bilpublishing.com/index.php/jmmr

ARTICLE

Health Risks of Trace Metals in Wastewater-Fed Fishes: A Case Study

Aslıhan Katip*

Bursa Uludag University, Faculty of Engineering, Department of Environmental Engineering, 16059, Bursa, Turkey

ARTICLE INFO

Article history
Received: 17 February 2019
Accepted: 5 March 2019
Published Online: 19 April 2019

Keywords:
Aquaculture
Bioaccumulation
Bio-concentration Factor
Secondary Treatment
Transfer factor

ABSTRACT

In this study, the usage wastewater from secondary treatment in feeding fishes of *Carassius gibelio* species and suitability of the fishes for human food were evaluated. The metals (Ag, Al, As and B) in treated effluent and skeleton, skin, eyes and brain tissues of fishes were examined seasonally. It was found that treated effluent was not suitable for irrigation and aquaculture in terms of Al according to the Turkish standard values. According to annual averages the size order of Ag and B concentrations were skeleton> skin> eyes>brain and skeleton> skin>brain>eye respectively. Also, skin>brain>eyes>skeleton was for As and Al. TF (Transfer Factor) values of all metals examined were determined as >1 in the four tissues and the metals caused bioaccumulation because of treated effluent. Concentrations in muscles were found 7 to 6227 times higher than in water. The size order of TF and BCF (Bio-concentration Factor) values in skin and eye tissue were the same and it was Ag>Al>As>B. It was Ag>Al>As>B in skeleton, Al>As>Ag>B in brain. HQ (Hazard Quotient) of Al in all tissues had carcinogenic risk level.

1. Introduction

Serious water demand caused by population growth, urbanization and industrialization have been in the world [1]. Many countries are seeking reuse of waste waters for meeting their national water requirement [2].Sewage-fed aquaculture is a unique system and has manifold advantages in developing countries acting as a major source of nutrients for crop farming and aquaculture, economical for sustainable production and helps to combat environmental pollution [3]. In the urban swage wastewater is mixed with industrial wastewater. Even if sewage water is treated, its use in aquaculture has some health disadvantages because of its toxic chemicals and microbiological pollution. Especially, heavy metals are potentially harmful to most organisms at some level of exposure and absorption [4]. Most of the metals are absorbed into the body through respiration, digestion and skin. Metals could be found in high concentrations in the skeleton and skin tissues and can cross the brain wall [5, 6, 7] Brain tissues accumulated more heavy metal than edible muscle tissues.

The aims of this study were to evaluate the suitability of treated wastewater-fed fishes to health risk for human food consumption in terms of the metals of Ag, Al, As and B. This study may contribute valuable information for evaluating potential health risks of wastewater reuse as aquaculture feeding water were exist. This study was important to see the accumulation of metals in fish tissues due to feed with wastewater and the level of their cancer risks.

**Corresponding Author:*
Aslıhan Katip,
Bursa Uludag University, Faculty of Engineering, Department of Environmental Engineering, 16059, Bursa, Turkey;
Email: aballi@uludag.edu.tr

DOI: https://doi.org/10.30564/jmmr.v2i1.540

2. Material and Methods

2.1 Experimental Studies

In this study *Carassius gibelio* type fish grown in wastewater-fed ponds were caught seasonally and Ag, Al, As and B concentrations in skeleton, skin, eye and brain tissues were determined.

The fish ponds were fed with the effluent of East Wastewater Treatment Plant of Bursa City has the advanced biological treatment (five-stage Bardenpho). The volumetric flow is 240000 m^3/day for the year 2017 [8].

12 fish samples *of Carassius gibelio specie* were catched along the same year (2011-2012, 3 samples per season) from the fish breeding pool after last clarifier. The fishes were taken to laboratory in the polyethylene caps and their sizes were recorded. The fishes were cut from its backing with the help of stainless steel knife and muscle, liver, and gill tissues were removed. These tissues were then homogenized and 0.5 g (wet weight) were weighed and placed in constantly weighed petri dishes to dry for 24 hours in drying oven. Afterward, the tissue samples fixed to dry weight placed in to temperature and pressure-compensated HP500 Teflon caps. 7 ml nitric acid (HNO_3) and 1 ml hydrogen peroxide (H_2O_2) were added as reagents and the samples were digested by using CEM Mars 5 Model microwave instrument [9]. Microwave decomposition operations were programmed as a 3-phase process. The device operated at 5 psi (1 psi=6.89 kPa) for 1 minute in the 1st stage, at 25 psi for 5 minutes in the 2nd stage and at 120 psi for 60 minutes in the 3rd stage [10]. After the samples were cooled to room temperature and the samples were diluted to 50 ml by using ultra-pure water. Blanks and European standard reference materials (ERMBB422) were included in each digestion batch to verify the accuracy of the calibration and standardization method, and all analyses were done in duplicate.

The water samples were taken by using with Aquacell P2-COMPACT portable composite sampler then they were transferred to the dark polyethylene (PE) bottles washed with HNO_3 and deionized water [11]. All the samples were taken monthly along 1 year from January 2011 to 2012 in order to see the seasonal changes. Water samples were filtered through a Millipore filter paper with preweighed 0.45 µm pore-size. The filtered water samples were acidified with 0.2% (v/v) concentrated nitric acid as the precipitation samples and kept in glass bottles cleaned with detergent, water, nitric acid and Milli-Q water respectively [10]. Heavy metals and trace elements in water and fish tissues were determined using the VISTA-MPX model of the VARIAN brand ICP-OES device.

2.2 Metal Bioaccumulations and Assessment of Health Risk

The transfer and bio-concentration factors were calculated in order to determine metal bioaccumulation in fish tissues. The transfer factor in fish tissues from the aquatic ecosystem, which include water and sediments, was calculated according to Rashed (2001) [12] as follows:

$$TF = M_{tissue}\,(\text{mg/kg dry weight}) / M_{sediment\ or\ water}\,(\text{mg/L}) \quad (1)$$

And also bio-concentration factor as follows [13]:

$$BCF = M_{tissue}\,(\text{mg/kg wet weight}) / M_{water}\,(\text{mg/L}) \quad (2)$$

Where, M_{tissue} is the metal concentration in fish tissue; $M_{sediment}$, metal concentration in sediment. The concentrations in TF sediments were not used in this study because only the effect of water was examined.

BCF is based on water only exposures (lab data). BCF and TF are inversely related to exposure concentrations. BCF >1000 and TF >1 have been used to signify hazard in many national regulatory schemes. However hazard and potential for chronic effects cannot be just evaluated by magnitude of BCF [14]. TF, BCF and standard concentration values should be evaluated together. BCF has different values for each metal [13].

The risk for human health as a result of eating *Carassius gibelio* was evaluated by calculating estimated daily intake (EDI) using the following equation [15, 16]:

$$EDI = \frac{Cfish * Dfish}{BW} \quad (3)$$

Where C_{fish}= the average trace element concentration in fish muscle (µg/g dry weight), D_{fish}= the global average daily fish consumption (g/day) which was only 1.7 g/day for Turkey [17], and BW= average body weight (kg).

US-EPA risk analysis, considering an adult average body weight of 70 kg [18]. The Hazard quotient (HQ) was calculated by dividing the estimated daily intake (EDI) by the established RfD (reference dose) to assess the health risk from fish consumption. There would be no obvious risk if the HQ were less than 1 [15].

3. Results and Discussion

Metal (Ag, Al, As and B) concentrations in skeleton, skin, eye and brain tissues of *Carassius gibelio* species were determined in summer and winter. In skeleton and brain tissues, summer concentrations of Ag and As were higher than winter values. Winter concentrations of Al and B were higher than summer values in these tissues. In winter Ag, Al and As concentrations of eye tissues higher

DOI: https://doi.org/10.30564/jmmr.v2i1.540

than winter values but B concentrations of eye in winter higher than summer values. In skin tissues, winter concentrations of As, Al and B higher than summer, also Ag in summer higher than winter concentrations. The concentrations in the skeleton and brain showed similar seasonal changes.The seasonal metal concentrations in skeleton, skin, eye and brain tissues were shown in Figure 1.

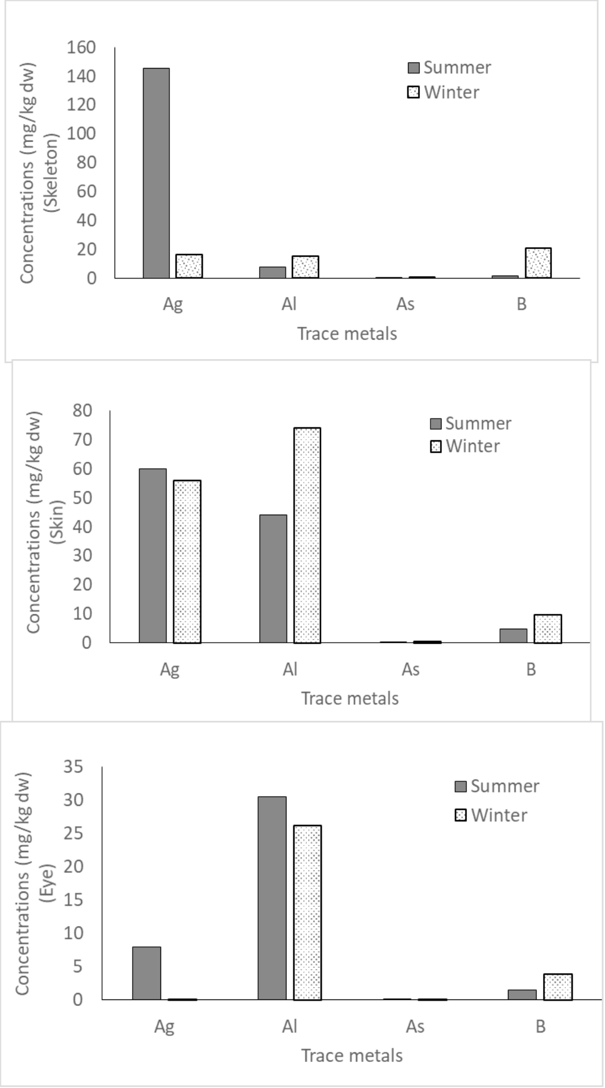

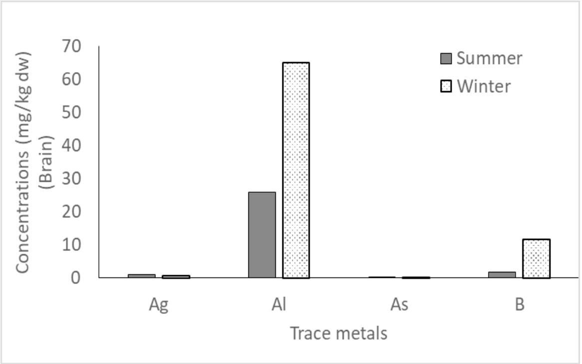

Figure 1. The seasonal metal concentrations in skeleton, skin, eye and brain tissues

According to annual averages the size order of Ag and B concentrations were skeleton> skin> eye>brain and skeleton> skin>brain>eye respectively. Also skin>brain>eye>skeleton was for As and Al. Higher concentrations were found in skeletal and skin tissue. Higher concentrations in skeletal and skin tissue were found than the other tissues. It was determined that metal accumulation was found in nervous system.In different studies, B concentrations in fish head were higher than muscle, liver and gill [19]. It was determined that Cd concentration in skeleton was higher than skin, muscle and gill tissues and Ni concentrations in skeleton, brain and skin tissues were found close to each other [5]. Adebayo, et. al., 2017 was found that Zn, Pb and Fe in brain higher than eye [6]. Cd, Pb, Cu, Zn and Mn in skeleton were higher than skin concentrations [20]. Yin, et. al., 2018 was studied with 8 different fish species and metal concentrations in internal organs were determined higher than edible muscle tissue [21]. The annual averages of the metal concentrations in the tissues were given in Table 1.

According to the Turkish food codex annual averages of As concentration in all tissue were above the standard value [22]. National and international standard concentration values of other metals are not exist for fishes. There are daily intake doses of these metals [15, 19]. For this rea-

Table 1. Annual average of the metal concentrations in the tissues

Metals	Skeleton (mg/kg)		Skin (mg/kg)		Eye (mg/kg)		Brain (mg/kg)	
	Wet weight	Dry wight	Wet weight	Dry wight	Wet weight	Dry wight	Wet weight	Dry wight
As	0.04245±0.0078	0.0604± 0.011	0.07975± 0.010	0.3065± 0.0415	0.02015± 0.015	0.077± 0.061	0.05255± 0.025	0.2625± 0.129
B	7.73285±6.697	11.0465± 9.567	1.889± 0.642	7.265± 2.469	0.687± 0.305	2.642± 1.173	1.317± 0.987	6.585± 4.935
Al	7.872±2.683	11.245± 3.833	15.3605± 3.926	59.078± 15.102	7.3635± 0.566	28.321± 2.179	9.075± 3.914	45.375± 19.57
Ag	56.66± 45.254	80.9545± 64.649	15.0825± 0.505	58.009± 1.944	1.0585± 1.023	4.0705± 3.936	0.16± 0.044	0.8±0.22

son, health risk was determined by calculating the values of the hazard quotient, transfer and bio-concentration factors.

Annual mean of Ag, Al, As and B concentrations of treated effluent water were 0.013, 0.3383, 0.0033 and 0.3393 mg/L respectively. TF (Transfer Factor) values of all metals examined were observed as >1 in the four tissues and the metals caused bioaccumulation because of treated effluent. Concentrations in muscles were found 7 to 6227 times higher than in water. Size order of TF and BCF (Bio-concentration Factor) values in skin and eye tissue were the same and Ag>Al>As>B. They were Ag>Al>As>B in skeleton and Al>As>Ag>B in brain. HQ (Hazard Quotient) of Al in all tissues had carcinogenic risk level. Because Ag, As and Al except than Boron are not essential elements [19] excess of this element's concentrations caused toxic effect for fishes and humans. Calculated hazard quotient, transfer and bio-concentration factors were given in Table 2. Although treated wastewater was used in aquaculture and irrigation in many countries [23, 24, 25], it was observed that Bursa urban wastewater cannot be used for aquaculture.

Table 2. Calculated hazard quotient, transfer and bio-concentration factors

Metals	US EPA (1999) BCF (L/kg)	RfD	Skeleton				Skin				Eye				Brain			
			TF(L/kg)	BCF (L/kg)	EDI (µg/kg b.w/gün)	HQ	TF(L/kg)	BCF (L/kg)	EDI (µg/kg b.w/gün)	HQ	TF(L/kg)	BCF (L/kg)	EDI (µg/kg b.w/gün)	HQ	TF(L/kg)	BCF (L/kg)	EDI (µg/kg b.w/gün)	HQ
As	114	0,3	18	12	0,001	0.003	92	24	0.007	0.023	23	6	0.001	0.003	79	15	0.006	0.02
B	–	–	32	22	0.268	–	21	5	0.176	–	7	2	0.064	–	19	3	0.159	–
Al	76	0.025	33	23	0.273	10.920	174	45	1.434	57.36	83	21	0.687	27.48	134	26	1.11	44.04
Ag	–	5	6227	4359	1.966	0.393	4462	1160	1.408	0.281	313	81	0.098	0.019	61	12	0.019	0.003

4. Conclusions

This study showed that wastewater treated with advanced purification may not be appropriate with regard to aquaculture for metal parameters. It was determined that Ag, Al, As and B caused the bioaccumulation in skeleton, skin, eye and brain tissues in this study. TF and BCF (Bio-concentration Factor) values in skin and eye tissue showed a similar trend and Al in all tissues had carcinogenic risk level. These results were important to see the levels of metal accumulation in fish tissues and to show that the usage of treated urban wastewater for aquaculture could be harmful.

In the future bioaccumulations of different micro-pollutants in varied fish species must be research. Also, there are no guideline values or provisional limits for metal intake (g/day/body weight), the results obtained in this study could be used to derive such guideline values. However, this needs to be further examined in future studies. Reuse of wastewater will become more important in the future due to water scarcity.

References

[1] Scheumann, W., Kibaroglu, A., Kramer, A. Turkey's Water Policy National Frameworks and International Cooperation, Springer, 2011.

[2] Hermanowicz, S.W. Is Scarcity a Real Driver for Water Reuse?. University of California, Berkeley, CA 94720-1710, 2006.

[3] Gisecke, U., Heiland, S., Million, A., Junge, R. Urban Aquaculture, Deutsche National Bibliothek, Berlin, 2014.

[4] Kumar B., Mukherjee D.P., Kumar S., Mishra M., Prakash D., Singh K., Sharma C.S. Bioaccumulation of Heavy Metals in Muscle Tissue of Fishes from Selected Aquaculture Ponds in East Kolkata Wetlands. Annals of Biological Research, 2011, 2 (5):125-134.

[5] Abubakar, A., Uzairu, A., Ekwumemgbo, P. A., Okunola, O. J. Risk Assessment of Heavy Metals in Imported Frozen Fish Scomber scombrus Species Sold in Nigeria: A Case Study in Zaria Metropolis, Advances in Toxicology, 2015, 2015, ID 303245: 1-11.

[6] Adebayo, I. A., Determination of Heavy Metals in Water, Fish and Sediment from Ureje Water Reservoir, Journal of Environmental & Analytical Toxicology, 2017, 7 (4): 1-4.

[7] Yavuz, C.I., Vaizoglu, S. A., Güler, Ç., Aluminium in Drinking Water, TAF Preventive Medicine Bulletin, 2013, 12 (5): 589-596.

[8] BWS. Bursa Water and Sewerage Administration, the Head of Wastewater Treatment Department, 2018. http://www.buski.gov.tr/tr/icerik/dogu_atik_su_aritma_tesisi_575

[9] Uysal K., Köse E., Bülbül M., Dönmez M., Erdoğan Y., Koyun M., Ömeroğlu Ç., Özmal F. The comparison of heavy metal accumulation ratios of some fish species in Enne Dame Lake (Kütahya/Turkey). Environ Monit Assess, 2009, 157: 355–362.

[10] Benzer, S., Aralan, H., Uzel, N., Gül, A. Yilmaz, M. Concentrations of metals in water, sediment and tissues of Cyprinus carpioL., 1758 from Mogan Lake (Turkey), Iranian Journal of Fisheries Sciences, 2013, 12(1): 45-55.

[11] Apha Awwa Standard Methods for the Examination of Water and Wastewater. American Public Health Association, 23rd Edition. Washington DC USA, 2017.

[12] Rashed, M.N. Monitoring of environmental heavy metals in fish from Nasser Lake, Environment Inter-

DOI: https://doi.org/10.30564/jmmr.v2i1.540

national, 2001, 27: 27-33.

[13] USEPA. Screening Level Ecological Risk Assessment Protocol for Hazardous Waste Combustion Facilities. United States Environmental Protection Agency EPA530-D-99-001C, 1999.

[14] OECD. Bioaccumulation of Metal Substances by Aquatic Organisms Part 1. OECD Meeting, Paris, 2011.

[15] Onsaint S., Ke C., Wang K.J., Wang W.X. Trace elements in two marine fish cultured in fish cultured in fish cages in Fujian province, China. Environ. Pollut. 15:1334-1345.2010.

[16] Ekeanyanwu R.C., Nwokedi C.L., Noah U.T. Monitoring of Metals in Tilapia Nilotica Tissues, Bottom Sediments and Water from Nworie River and Oguta Lake in Imo State, Nigeria. African Journal of Environmental Science and Technology, 2015, 9 (8): 682-690.

[17] Sarıözkan S. Türkiye'de Balıkçılık Sektörü ve Ekonomisi. Turkish Journal of Aquatic Sciences, 2016, 31(1):15-22.

[18] Mol, S., Karakulak, F.S., Ulusoy, S. Assessment of Potential Health Risks of Heavy Metals to the General Public in Turkey via Consumption of Red Mullet, Whiting, Turbot from the Southwest Black Sea, Turkish Journal of Fisheries and Aquatic Sciences, 2017, 17: 1135-1143.

[19] Emiroğlu Ö., Çiçek A., Arslan N., Aksan S., Rüzgar M. Boron Concentration in Water, Sediment and Different Organisms around Large Borate Deposits of Turkey. Bull Environ Contam Toxicol, 2010, 84:427–431.

[20] Asmah, R., Biney, C. A. Distribution of heavy metals in tissues and organs of tuna. International Journal of Fisheries and Aquatic Studies, 2014, 1(6): 82-86.

[21] Yin, J., Liu, Q., Wang, L., Li, J., Li, S., Zhang, X. The distribution and risk assessment of heavy metals in water, sediments, and fish of Chaohu Lake, China, Environmental Earth Sciences, 2018, 77: 97.

[22] TFC. Turkish Food Codes, - Maximum Limits of Contaminants in Foodstuffs. Official Gazette, 2011, 28157.

[23] Katip, A. Reuse of Treated Wastewater (in Science, Ecology and Engineering Research in the Globalizing World, Efe, R. (eds.)), St. Kliment Ohridski University Press, Sofia, 2018.

[24] Katip, A. Evaluation of Treated Wastewater Reuse Areas, Omer Halisdemir University Journal of Engineering Sciences, 2018, 7 (2): 541-557.

[25] Das, S. K., Mandal, A. Waste System: Its Utility and Analyses in Aquaculture (in Wastewater Management Through Aquaculture, B. B. Jana et al. (eds.)),Springer Nature Singapore Pte Ltd., 2018.

BILINGUAL PUBLISHING CO.
Pioneer of Global Academics Since 1984

Journal of Metallic Material Research
https://ojs.bilpublishing.com/index.php/jmmr

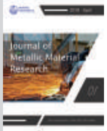

ARTICLE

Influence of the M and M' Metals on the Carbides Population in As-Cast M'-based Alloys Designed to be MC-Strengthened

Patrice Berthod[*]

University of Lorraine, Institut Jean Lamour, Campus Artem, 2 Allée André Guinier 54000 Nancy, France

ARTICLE INFO

Article history
Received: 8 March 2019
Accepted: 28 March 2019
Published Online: 19 April 2019

Keywords:
Cast refractory alloys
MC carbides
As-cast microstructures
Base element
monocarbides-former elements

ABSTRACT

High temperature applications such as turbine blades for aeronautics or molten glass-shaping tools require the use of refractory metallic materials. Among the later ones, cast superalloys based on some transition metals and reinforced by MC carbides stay in good place and their metallurgy merits to be well known. This work consists in a general exploration of the as-cast microstructures which can be obtained after solidification and solid state cooling down to ambient temperature for a wide series of alloys for which the base element and the MC-former element both vary. For fixed contents in chromium and carbon contents, the compositions of a total of nineteen alloys were considered. These alloys are based on Ni, Co, Fe or Nb and the M content was each time chosen to favor the appearance of TiC, TaC, NbC, HfC or ZrC, as single carbide in a given alloy. After elaboration, metallographic samples were observed by electron microscopy to investigate the obtained microstructures. The obtained results show first that the MC carbides were in many cases successfully obtained at the expense of other possible carbides (for all Co-based alloys for example) but there are also several exceptions (notably for some Ni-based alloys). Second, the obtained monocarbides have a eutectic origin and they are script-liked shaped. However they are here too some exceptions, as the rare HfC obtained in a Nb-base). In general, the results obtained in this work show that the principle of dendritic matrix combined with MC carbides with a script-like morphology is not necessarily obtained: the nature of the {base element, MC-former element} combination governs the microstructure of the alloy in its as-cast state for these particular compositions in chromium and carbon. In some cases other carbides may appear and the microstructures may be even of another type.

1. Introduction

Superalloys are used since several decades in industry aeronautics (notably as turbine disks and blades), power generation (such as burners and hottest parts of turbines) and industries involving processes working at elevated temperature (e.g. tools for shaping molten glasses) [1]. During the past decades their usage became more and more expanded because of the increase in efficiency demand [2]. The initial superalloys were elaborated by classical foundry processes [3] but new elaboration routes for these high performance refractory metallic materials appeared. These ones are more (Powder Metallurgy [4,5], single crystalline solidi-

---

**Corresponding Author:*
Patrice Berthod,
University of Lorraine, Institut Jean Lamour, Campus Artem, 2 Allée André Guinier 54000 Nancy, France;
Email: patrice.berthod@centraliens-lille.org

DOI: https://doi.org/10.30564/jmmr.v2i1.604

fication [6,7] …) or less (additive manufacturing [8,9] …) classic. Although their elaboration techniques are rather old [10, 11], foundry processes leading to polycrystalline and equiaxed microstructures still possess high interest for obtaining highly performant superalloys for applications at high temperature. Indeed, some chemical compositions and the resulting microstructures lead to very high melting start temperature (over 1300°C), high level of strength of the matrix (austenitic, dendritic), efficient strengthening of the matrix (solid solution and/or precipitation hardening) and strong particles useful for the interdendritic cohesion (e.g. script-like eutectic carbides). An important example may be given by an equiaxed chromium-containing cobalt-based alloy owning a dendritic matrix and taking benefit from interdendritic carbides closely imbricated with the periphery of the dendrites. Such an alloy possesses a continuous austenitic matrix with good hardness and high intrinsic mechanical resistance, moreover able to efficiently drive chromium toward the oxidation front to combat hot corrosion. Its interdendritic cohesion is favored by the script-like shape of the TaC carbides interlocking neighbor dendrites. The Mar-M 509 superalloy (commercial alloy from Martin-Marietta) globally corresponds to this description [1,11] despite the simultaneous presence of chromium carbides and TaC carbides (microstructure type similar to the one of the alloy showed in Figure 1). Another industrial alloy [12], despite the presence of nickel added to better stabilize the austenitic crystal structure of the matrix, corresponds more to this microstructural principle which led to remarkable performances at high temperatures under mechanical stresses and chemical aggressiveness.

The interest for MC carbides in alloys devoted for uses in severe conditions thus exists from several decades but this type of carbides is nowadays still considered for several types of alloys synthesized from various ways (sintering, solidification, coatings deposit…), ion cobalt-based [13, 14], iron-based [15], nickel-based [16, 17] and even High Entropy Alloys [18]. However alloy design involving MC carbides is rarely based on the exclusive presence of MC in the microstructure in which other carbides and other strengthening particles are present too. Obtaining in an alloy carbides which are only of the MC type is possible by correctly rating the contents in M and C. For instance tantalum monocarbides were successfully obtained as the single carbide present in one of the industrial alloys cited just above. This was successfully achieved thanks to both a good atomic correspondence between C and Ta and to the high thermodynamic stability of TaC in a cobalt-chromium environment. One can logically imagine that this $\{\%_{at}\,M=\%_{at}\,C\}$ condition may lead to the same results in other bases, for example involving nickel, iron… Other monocarbides-former elements such as Ti or Nb for example, which are stronger carbide-former elements than chromium [19], may be also considered. Thanks to their very high stability at elevated temperatures [20] one can expect exceptional high temperature properties in some cases, as this was already observed recently with the association of a polycrystalline dendritic Ni(Cr) matrix with eutectic HfC carbides: a matrix efficiently resisting hot oxidation/corrosion and morphologically highly stable script-like HfC interdendritic skeleton allowing high creep-resistance [21].

To check this, a study was initiated for several {M, M'} combinations, the M base element being Co, Ni Fe and Nb and the M' monocarbide-former element being Ti, Ta, Nb, Hf or Zr. Several recent results [22-25] were gathered and new alloy elaborations and microstructure characterizations were carried out to complete a collection based on 0.4-0.5 wt.%C and containing the corresponding M atomic contents for a molar {M=C} equivalence. A series of about twenty different alloys were thus obtained and taken into account in this study devoted to a metallurgical principle which is until today not yet recognized as competitor for g/g single crystalline superalloys despite its really great potential for applications gathering mechanically and chemically severe conditions of work for the used metallic pieces.

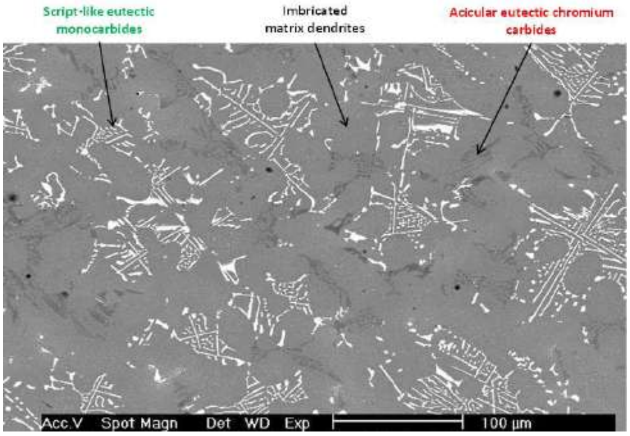

Figure 1. Microstructure of a Co(bal.)-9Ni-28Cr-1C-6Ta alloy

Note: It contains simultaneously some undesirable carbides (acicular eutectic chromium carbides) and the wished type of carbides: script-like eutectic MC carbides.

2. Methodology

2.1 Elaboration of the Alloys

All the alloys were issued from the mixing of initially

DOI: https://doi.org/10.30564/jmmr.v2i1.604

pure elements. Thus, small parts of pure Co, Ni, Fe, Nb, Cr, C (graphite), Ti, Ta, Hf and Zr (purity > 99.9 wt.%, graphite: 100%) were provided by Alfa Aesar and Aldrich. They were weighed with accuracy to obtain final charges with the following contents:

(1) $25 \leq Cr \leq 35$ wt.% and $0.4 \leq C \leq 0.5$ wt.%

(2) Ti, Ta, Nb, Hf and Zr: weight fractions chosen to have the same molar content as C (approximately: Ti close to 2 wt.%, Ta and Hf each close to 7.5 wt.%, Nb close to 4 wt.%, Zr close to 3wt.%)

(3) Co, Ni, Fe and Nb (if base element): balance

(4) Ingots masses: 40g for the Ni-based, Co-based and Fe-based alloys; 10g for the Nb-based alloys

The mixed elements corresponding to a final alloy were all placed together in a metallic crucible present in a high frequency induction furnace (CELES, France; power: 50kW). This copper-made crucible was continuously cooled by circulating water at ambient temperature during the elaboration steps.

After the introduction of the mix of pure elements, a silica tube was placed around the crucible and closed to allow the evacuation of the present air, by pumping it. The crucible and silica tube were surrounded by a copper coil (water–cooled too) through which an alternative current will circulate. The frequency of this alternative current was between 100 and 150 kHz, and the applied voltage was between 4 and 5kV, this depending on the alloy. After 3 cycles made of pumping until 5×10^{-5} bars followed by filling by pure Argon, the inside obtained atmosphere was considered as being of pure Ar, with a pressure rated at about 400 mbars.

Heating led to the melting of the charges made of pure elements and the obtained liquid alloy was maintained at the highest reached temperature during several minutes to achieve total chemical homogeneity. During the cooling, operated by decreasing the input power/voltage, the alloys started solidifying, and later cooled in solid state. After about 20 to 30 minutes after the end of isothermal stage in the liquid state, the obtained ingots were again at room temperature. They were then extracted from the crucible (Figure 2).

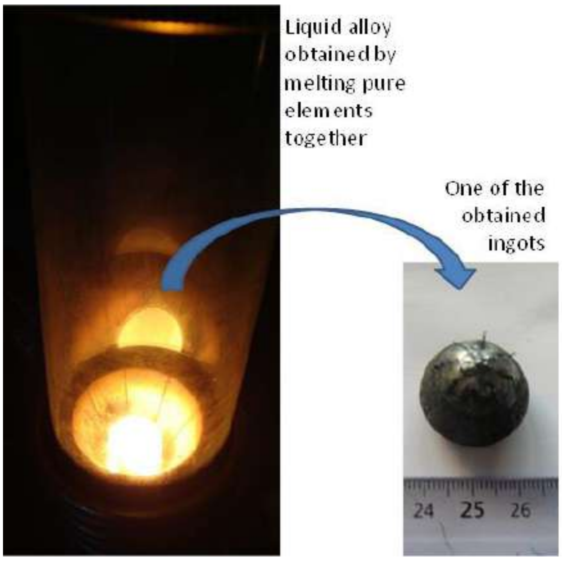

Figure 2. Illustration of the elaboration of the alloys for the study (high frequency induction melting and solidification in a cooled copper crucible)

2.2 Metallographic Characterization and Hardness Measurements

Each ingot was first cut using a metallographic saw. This allowed extracting a part of alloy which was embedded in a cold resin + hardener mixture (ESCIL, France). After total stiffening of the embedding resin the obtained samples were extracted from their plastic molds. They were ground by using first #120 or #240-grade SiC papers, then finished by #1200 or #2400-grade papers. Polishing was carried out using a textile disk enriched with 1 µm hard particles.

The obtained mirror-like samples were put, one by one, in the chamber of a Scanning Electron Microscope, model JSM-6010LA (JEOL, Japan). Their microstructures were observed in Back Scattered Electrons mode (acceleration voltage: 20kV), at different magnification ratings. Energy Dispersive Spectrometry was used to control the obtained chemical compositions by full frame analysis. Additionally, spot analyses were performed on the visible particles to try identifying them and to specify the chemical composition of the matrix. X-ray diffraction was also carried out for most of the studied alloys. This was done using a Philips X-Pert Pro diffractometer.

The metallographic samples were also subjected to indentation tests to assess the hardness of all alloys. This was carried out using a Testwell Wolpert indentation machine, according to the Vickers method. The applied loads were adjusted to the apparent hardness of the alloys: 10kg for the less hard ones and 30kg for the hardest ones. In the cases where possible fracture may happen because of crit-

DOI: https://doi.org/10.30564/jmmr.v2i1.604

ical lack of toughness 10kg was preferred at the expense of 30kg for some of the hardest alloys.

3. Results

3.1 Machinability and Hardness

The first observation concerns the cutting of the ingots. Cutting was rather easy for the Ni-based and Fe-based alloys. In an opposite way this was more difficult for the cobalt-based alloys. The highest difficulties of cutting were met for the niobium-based alloys: long time of cutting although the size of these ingots were small, intensive heating of the ingot and the cutting tool… This was obviously in relation with hardness. The indentation tests showed that this is the matrix nature which governs the room temperature hardness of these alloys, more than the type of carbide. About 200 Hv was found for all the nickel-based alloys and iron-based alloys, against around 350 Hv for all the cobalt-based alloys, and around 900 Hv for all the niobium-based alloys. These three levels of hardness globally correspond to the three difficulty levels of cutting.

3.2 Results of X-ray Diffraction Runs and of the Global Composition EDS Measurements

The most often, the peaks really visible in the XRD diffractograms concern the matrixes of the alloys. All the nickel-based alloys own a Face Centered Cubic (FCC) matrix. The matrixes of the cobalt-based alloys are generally composed of a mix of a FCC part and of a Hexagonal Compact part. The ones of the iron-based alloys were all Body Centered Cubic, (BCC). Concerning the niobium-base alloys, they were composed of two major phases: a Nb-based BCC phase and a Cr_2Nb phase with two crystalline structures (BCC and Hexagonal). In contrast, the diffraction peaks corresponding to the carbides were very small by comparison with matrixes, because of their low volume fractions. If this was possible in some cases (e.g. cobalt-based alloys, Figure 3), this was sometimes impossible to specify the presence of some carbides by this way (e.g. niobium-based alloys, Figure 4).

The full frame Energy Dispersion Spectrometry analyses allowed to verify that the targeted chemical compositions of alloys were all well respected. However, this concerns only the elements heavy enough, as is to say all of them except carbon.

3.3 SEM/BSE Microstructure Observations for the Ni-based Alloys

The as-cast state microstructures of the five nickel-based alloys are illustrated in Figure 5. Two successful MC formations were observed (left column): HfC in the Ni-25Cr-0.5C-5.6Hf alloy, and ZrC in the Ni-25Cr-0.5C-3.8Zr one. In both cases these carbides are the single carbide present, with the required location (interdendritic) and morphology (script-like mixed with the periphery of the dendrites). Other MC carbides were also obtained in two other cases but not as the single carbide phase present: TaC (respectively NbC) get along with chromium carbides (dark/black carbides) in the Ni-25Cr-0.4C-6Ta (resp. Ni-25Cr-0.5C-3.9Nb) alloy. The last nickel-based alloy (the one containing Ti) does not contain any TiC carbides but only chromium carbides.

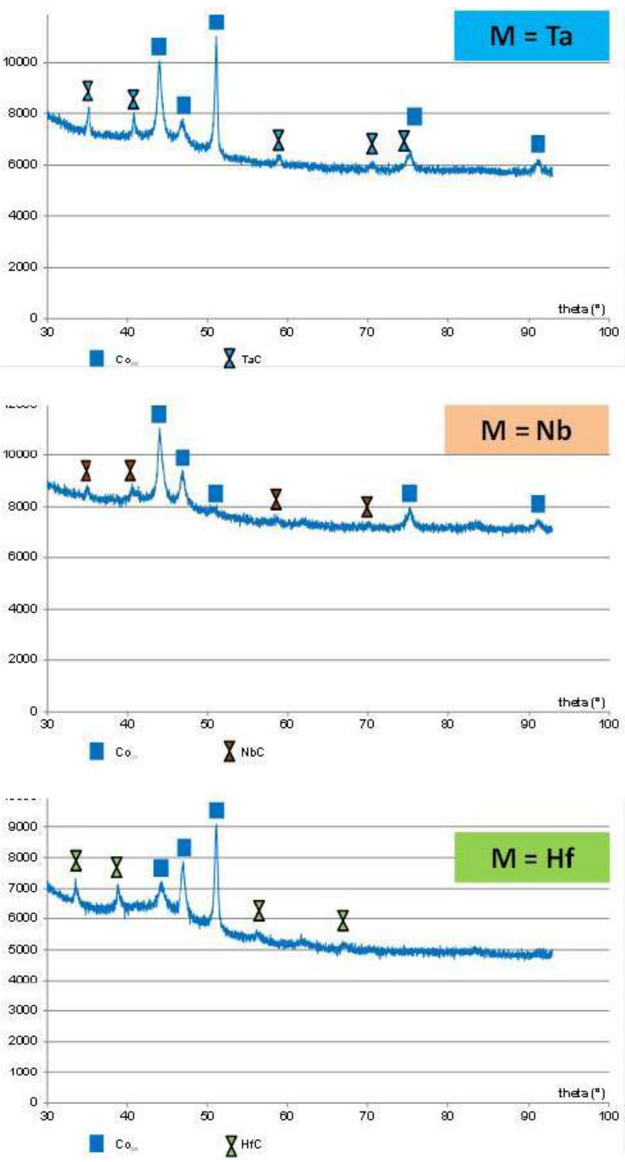

Figure 3. Three examples of XRD diffractograms allowing the identification of the carbides present (cobalt-based alloys with M=Ta (top), Nb (middle) and Hf (bottom) for forming MC carbides)

DOI: https://doi.org/10.30564/jmmr.v2i1.604

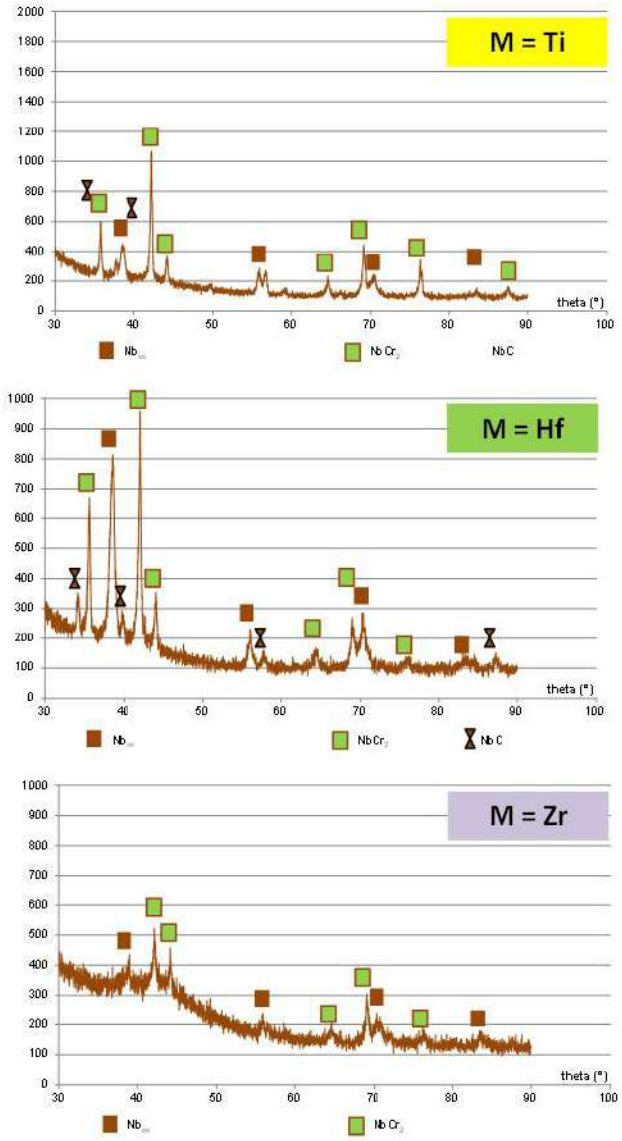

Figure 4. Three examples of XRD diffractograms from which the identification of the carbides present is not possible (niobium-based alloys with M=Ti (top), Hf (middle) and Zr (bottom) for forming MC carbides)

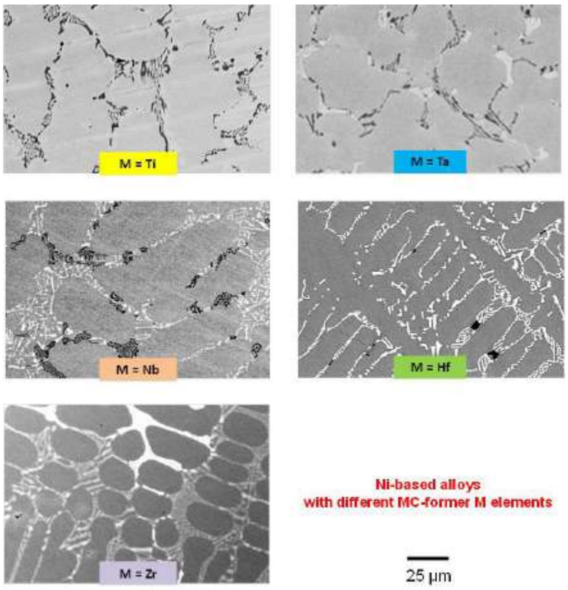

Figure 5. As-cast microstructures obtained for the Ni-based alloys with the different MC-former elements; SEM/BSE micrographs

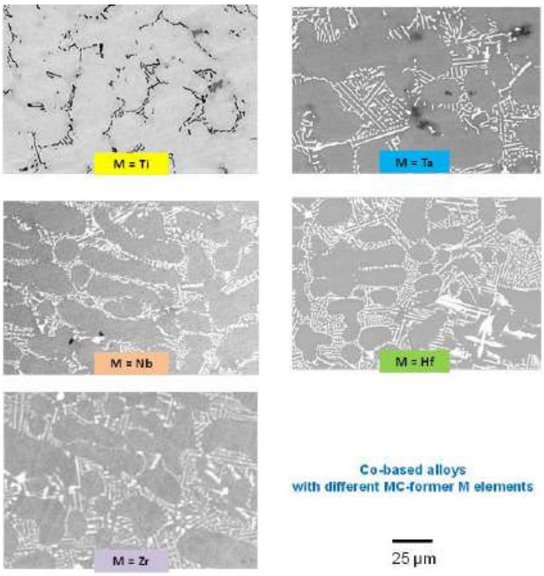

Figure 6. As-cast microstructures obtained for the Co-based alloys with the different MC-former elements; SEM/BSE micrographs

3.4 SEM/BSE Microstructure Observations for the Co-based Alloys

As illustrated by the micrographs presented in Figure 6, a cobalt-chromium base is particularly suitable to obtain MC carbides as single carbide phase present. In addition the wished morphologies and locations for the MC carbides were successfully obtained. Black script-like eutectic TiC carbide well precipitated during the solidification end of the Co-25Cr-0.5C-2Ti alloy. Similar results were obviously obtained for the bright TaC, NbC, HfC and ZrC carbides respectively in the Co-25Cr-0.4C-7.5Ta, Co-25Cr-0.5C-3.9Nb, Co-25Cr-0.5-7.4Hf and Co-25Cr-0.5C-3.8Zr alloys. However one must note that some rare and small chromium carbides appeared in some cases while the origin of the obtained MC carbides was not exclusively eutectic for some of these alloys. Notably, the Co-25Cr-0.5C-7.4Hf, which is rich in script-like eutectic HfC carbides, also contains some dispersed blocky HfC carbides, not specifically located in the interdendritic spaces. The later ones can be suspected to have appeared at the early stage of solidification, as a pre-eutectic carbide phase.

DOI: https://doi.org/10.30564/jmmr.v2i1.604

3.5 SEM/BSE Microstructure Observations for the Fe-based Alloys

The as-cast microstructures of the iron-based alloys are presented in Figure 7. Obtaining MC carbides in their as-cast microstructures was generally successful but not as systematic as for the cobalt-based alloys. First TiC carbides were not the single carbide present in the Fe-25Cr-0.5C-2Ti alloy since many chromium carbides appeared too. For the alloys containing exclusively – or at least mainly – MC carbides, the script-like shape was really obtained only for the Fe-30Cr-0.4C-6Ta alloy (eutectic TaC) and for the Fe-25Cr-0.5C-3.9Nb alloy (NbC). The HfC and the ZrC obtained in the Fe-25Cr-0.5C-5.6Hf alloy and the Fe-25Cr-0.5C-3.8Zr one, respectively, are more discontinuous. They are made of elongated particles without apparent contact between them.

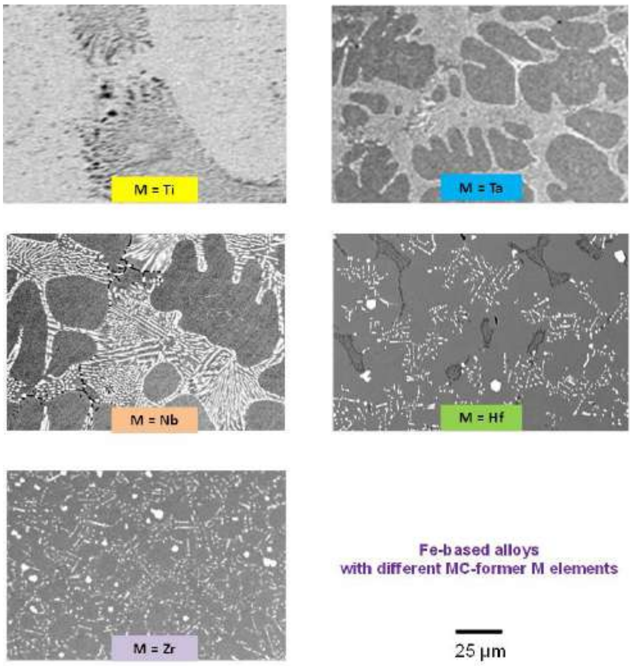

Figure 7. As-cast microstructures obtained for the Fe-based alloys with the different MC-former elements; SEM/BSE micrographs

3.6 SEM/BSE Microstructure Observations for the Nb-based Alloys

The niobium-based alloys behaved totally differently to the previous alloys families (Figure 8). The microstructures of three of them (Nb-33Cr-0.4C-1.6Ti, Nb-30Cr-0.4C-5.9Ta and Nb-33Cr-0.4C-2.9Zr) are characterized by the presence of dendrites of BCC Nb-based matrix and of a seemingly eutectic interdendritic compound made of BCC Nb-phase and Cr_2Nb Laves phase. No carbides seem existing in these alloys but the presence of some rare black particles must be noticed even if it is impossible to specify them taking into account their extremely small size. The Nb-33Cr-0.4C-5.8Hf alloy seems to be a little different from these three alloys since it contains less pre-eutectic BCC Nb-phase (which is maybe no dendritic) and more {BCC Nb-phase & Cr_2Nb}–made eutectic compound. MC carbides are obviously present in this later alloy, but with totally different morphology and location if compared to the alloys of the three other families. Here HfC are round and small, and seem systematically attached to the Nb-phase globules, or inside them.

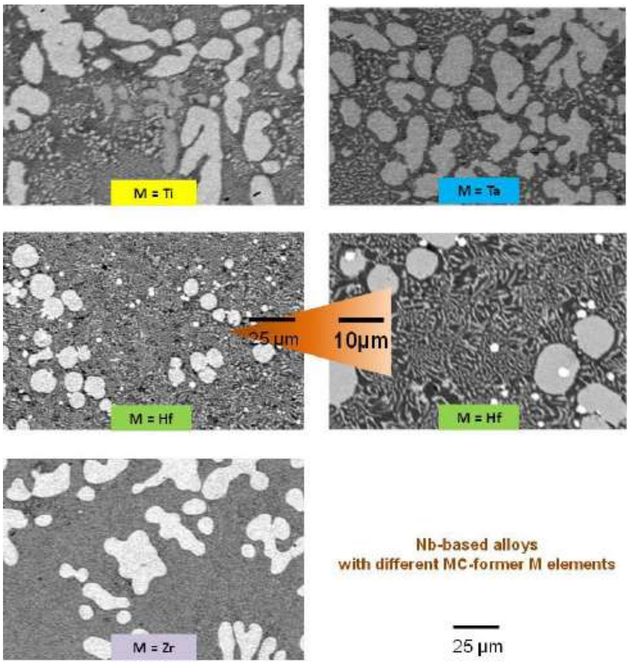

Figure 8. As-cast microstructures obtained for the Nb-based alloys with the different MC-former elements; SEM/BSE micrographs

4. Discussion

MC are among the most thermodynamically stable carbides [19]. They are known to precipitate at solidification or during solid state isothermal stages at high temperature in some superalloys containing MC-former elements and carbon with adequate contents, at the expense of other types of possible carbides. For instance, the presence of C in atomic excess by comparison with Ta leads to significant precipitation of eutectic TaC in the cast cobalt-based Mar-M 509 superalloy [1], while another cobalt-based superalloy used in industry [12] is strengthened by an interdendritic carbide network made of exclusively TaC thanks to the atomic equivalence between Ta and C in its chemical composition. The predominance of different MC carbides by the same choice of M and C atomic contents was rather recently explored in the case of cobalt-chromium alloys [20]. This allowed verifying that MC carbides form at the expense of all other types of carbides in such base.

This result was found again here with the five studied chromium-containing alloys based on cobalt. However one can see with the present work that results are much more contrasted with the three other alloys systems. The iron-chromium alloys effectively contain principally MC carbides when M is Ta, Nb, Hf or Zr, but with morphologies not strictly similar to the TaC ones (i.e. script-like) in cobalt-chromium alloys. It is not sure that the resulting of mechanical strengthening at high temperature can be of a level as high as for cobalt alloys. Furthermore, the ferritic structure of the matrix of these iron-based alloys is mechanically weak at high temperature, due to its low crystalline compactness. Concerning the nickel-based alloys, TiC, TaC and NbC meet the concurrence of chromium carbides, with as result a co-existence of MC and Cr_xC_y in the microstructure, and even a total absence of MC in some cases (i.e. for Ti). In such case the M element stays with rather high content in solid solution in the matrix, and even all the M atoms can be stocked in the matrix when no MC formed. This was verified here, for example for Ti in the nickel-chromium alloy by EDS spot analyses. Even when MC formed as single carbide for a chemical composition designed to respect the molar equivalence between M and C, a significant part of M may be present in solid solution in the matrix. This was the case here for instance for tantalum in the Co-25Cr-0.5C-7.4Ta in which the matrix contained almost 2 wt.% of the 7.4wt.% of Ta of the alloy. In this later case carbon atoms were automatically present in solid solution in the matrix of this alloy. In contrast, Hf was never present in solid solution in the matrix of the alloys, regardless of the base element among Ni, Co and Fe. In contrast, as for Ta, Ti and Zr, Hf was present in significant quantity (several wt.%) in the Nb-phase and in the Cr_2Nb phase.

If cobalt played here a particular role by allowing the systematic formation of the wished MC carbides exclusively, hafnium acted itself as a constant MC-former element since it was always present in the alloys of this work containing Hf. The molar equivalence of Hf and C led to the formation of carbides made of exclusively HfC in the Ni-based, Co-based and Fe-based alloys, while HfC was the only MC carbide to form with a visible presence in niobium-chromium alloys. Unfortunately no strengthening effect can be awaited from these small and round HfC particles formed in this Nb-33Cr-0.4C-5.8Hf alloy for high temperature uses.

The benefit of the script-like shape of MC carbides for the creep resistance at elevated temperature was demonstrated less [12, 26] or more [27] recently, by comparison between the deformation rates of alloys with a rather high fraction of MC carbides and alloys of the same compositions and tested in the same conditions with less such MC carbides or with chromium carbides instead.

5. Conclusion

The formation of MC carbides during the solidification of M-{25 to 35}Cr-{0.4 to 0.5}C-M’ alloys (M’: monocarbide-former element) is thus obviously more complex that the previous observations – limited to cobalt-chromium systems – allowed to think [28]. Chromium carbides may be unexpectedly thermodynamically favored in some cases and when MC successfully forms, this is not necessarily with the morphology which is the most favorable to high mechanical resistance at elevated temperature (TaC in Fe-30Cr alloys, [29]). The potentially best combinations for such objective are nickel-chromium with HfC and cobalt-chromium with any of the MC considered here. Although being an alloy system globally favorable to MC formation iron-chromium alloys risk to be handicapped by the intrinsic weakness of the ferritic structure of their matrixes. Regarding the niobium alloys, this is more the lack of ductility and of toughness [30] which would obstruct their use rather than the failure of precipitation of MC carbides during solidification.

This overview of all these as-cast microstructures which has allowed a preliminary exploration of the as-cast microstructures for a wide range of {M’(Cr) × MC-former element}- systems, must be now followed by thorough investigations for understanding the intrinsic differences of behavior between these metallurgical systems which lead to so evident microstructure differences between the different families for a given type of MC-former element and inside a given family for different MC-former elements. First results are currently available but numerous other phenomena remain to be explained.

Acknowledgement

my students in trainee period who worked with me in this research field: W. Abed, M. Bouaraba, J. Cai, E. Conrath, L. Corona, K. Duretz, L. Héricher, Y. Hamini, Z. Himeur, J.-P. Gomis, C. Heil, M. Khair, V. Kuhn, A. Leroy, A. Navet, G. Michel, S. Michon, S. Ozouaki, J. Peultier, G. Pierson, A.-S. Renck-Didelot, M. Ritouet-Léglise, S. Tlili, L. Toubal, C. Vébert

my colleagues for their technical help: L. Aranda, G.

Medjahdi, P.-J. Panteix, Th. Schweitzer, P.Villeger

References

[1] Chester T. Sims, Norman S. Stoloff, William C. Hagel “Superalloys II. High Temperature materials for aerospace and industrial power” John Wiley & Sons, 1987.

[2] Art Kracke “Superalloys, the most successful alloy system of modern times – Past, Present and Future”, in Proceedings of the 7th International Symposium on Superalloy 718 and Derivatives (Edited by: E. A. Ott, J. R. Groth, A. Banik, I. Dempster, T. P. Gabb, R. Helmink, X. Liu, A. Mitchell, G. P. Sjöberg and A. Wusatowska-Sarneck), TMS (The Minerals, Metals & Materials Society), 2010.

[3] Chester T. Sims, William C. Hagel “The Superalloys-Vital High Temperature Gas Turbine Materials for Aerospace and Industrial Power” John Wiley & Sons, New York, 1972.

[4] William Eisen, “Powder Metallurgy Superalloys”, Materials World, 1996, 4: 22-24.

[5] B. Paintendre, Y. Bienvenu, C. Ducrocq, J. C. Lautridou, J. H. Davidson, O. Faral “The influence of gamma prime forming elements on the properties of a nickel base superalloy produced by powder metallurgy” in the Proceedings of the “High Temperature Alloys for Gas Turbines and Other Applications 1986” Conference, Part I (Edited by W. Betz, R. Brunetaud, D. Coutsouradis, H. Fischmeister, T. B. Gibbons, I. Kvernes, Y. Lindblom, J. B. Marriott and D. B. Meadowcroft) Liège, Belgium, 1986: 867-876,

[6] Dedou Chen, Shuyue Wei, Zhontang Wu, Yafang Han “The creep behaviour of a nickel-base single crystal superalloy” in the Proceedings of the “High Temperature Alloys for Gas Turbines and Other Applications 1986” Conference, Part I (Edited by W. Betz, R. Brunetaud, D. Coutsouradis, H. Fischmeister, T. B. Gibbons, I. Kvernes, Y. Lindblom, J. B. Marriott and D. B. Meadowcroft) Liège, Belgium, 1986: 1441-1450,

[7] Matthew J. Donachie, Stephen J. Donachie “Superalloys: A Technical Guide” (2nd edition), ASM International, Materials Park, 2002.

[8] Benjamin Graybill, Ming Li, David Malawey, Chao Ma, Juan-Manuel Alvarado-Orozco, Enrique Martinez-Franco “Additive Manufacturing of nickel-based superalloys” in Proceedings of the ASME 2018 13th International Manufacturing Science and Engineering Conference MSEC2018, College Station, TX, USA, 2018: 1-17.

[9] Apoorv Kulkarni “Additive Manusfacturing of Nickel Based Superalloys”: 1-12. https://pdfs.semanticscholar.org/5455/29c63bc4b390a87d5fc0d3fd526ebfbfde4a.pdf

[10] G. Lamanthe, J. M. Theret, W. J. Boesch, G. E. Maurer “UDM 56: a new nickel base equiaxed superalloy”, in the Proceedings of the “High Temperature Alloys for Gas Turbines and Other Applications 1986” Conference, Part I (Edited by W. Betz, R. Brunetaud, D. Coutsouradis, H. Fischmeister, T. B. Gibbons, I. Kvernes, Y. Lindblom, J. B. Marriott and D. B. Meadowcroft) Liège, Belgium, 1986: 965-978

[11] Elihu F. Bradley, “Superalloys: A Technical Guide” (1st edition), ASM International, Metals Park (1988).

[12] P. Berthod, J.-L. Bernard, C. Liébaut “Cobalt-chromium alloy for spinner cups in manufacture of mineral wool from silicate glass”, International Patent, PCT Int. Appl, 2001: WO 2001090429 A1 20011129.

[13] S. H. Chang, C. C. Ko “Effects of MC carbide precipitates on the microstructure and mechanical properties of cobalt-based alloys adding TiC powder via vacuum sintering process”, Materials Transactions, 2013, 54(10): 399-404.

[14] S. H. Chang, C. C. Ko “Characterization of the MC carbides and mechanical properties in a TiC particles-strengthened cobalt-based alloy through HIP, solid-solution and aging treatments”, Materials Transactions, 2013, 54(3): 2049-2054.

[15] K. Nakama, K. Sugita, Y. Shirai “Effect of MC Type Carbides on Age Hardness and Thermal Expansion of Fe-36 wt%Ni-0.2 wt%C Alloy”, Metallography, Microstructure, and Analysis, 2013, 2(6): 383-387.

[16] W. Wang, R. Wang, A. Dong, G. Zhu, D. Wang, W. Zhou, W. Pan, D. Shu, B. Sun “Creep behaviors of MC carbide reinforced nickel based composite”, Materials Science & Engineering, A: Structural Materials: Properties, Microstructure and Processing, , 2019, 756: 11-17.

[17] W. Wang, G. Zhu, R. Wang, D. Wang, W. Pan, W. Zhou, D. Du, A. Dong, D. Shu, B. Sun “Novel in situ synthesized carbide reinforced Ni base composite for structural castings with high creep resistance”, Materials & Design, Ahead of Print, 2019.

[18] N. N. Guo, L. Wang, L. S. Luo, X; Z. Li, R. R. Chen, Y. Q. Su, J. J. Guo, H. Z. Fu “Microstructure and mechanical properties of in-situ MC-carbide particulates-reinforced refractory high-entropy Mo0.5NbHf0.5ZrTi matrix alloy composite”, Intermetallics, 2016, 69: 74-77.

[19] S. R. Shatynski “The thermochemistry of transition metal carbides”, Oxidation of Metals, 1979, 13(2): 105–118.

[20] P. Berthod “High temperature properties of several

chromium-containing Co-based alloys reinforced by different types of MC carbides (M= Ta, Nb, Hf and/or Zr)", Journal of Alloys and Compounds, 2009, 481: 746-754.
https://doi.org/10.1016/j.jallcom.2009.03.091

[21] P. Berthod, E. Conrath "Creep and oxidation kinetics at 1100 °C of nickel-base alloys reinforced by hafnium carbides", Materials and Design, 2016, 104: 27-36.
http://dx.doi.org/10.1016/j.matdes.2016.04.079

[22] E. Conrath, P. Berthod "Microstructure evolution at high temperature of chromium-rich iron-based alloys containing hafnium carbides", International Journal of Materials Research (formerly: Zeitschrift für Metallkunde), 105(8): 717-724.
https://doi.org/10.3139/146.111085

[23] P. Berthod, E. Kretz, F. Allègre "Experimental and thermodynamic study of the role of titanium in the microstructural and thermal properties of cast Ni–Cr–C–Ti alloys", Calphad, 2017, 56: 41-48.
http://dx.doi.org/10.1016/j.calphad.2016.11.008

[24] P. Berthod, M. Ritouet-Léglise "Microstructures and hardness of model niobium- based chromium-rich cast alloys", Advances in Materials Research, 2018, 7(1): 17-28.
https://doi.org/10.12989/amr.2018.7.1.017

[25] P. Berthod, M. Khair "Thermodynamic and experimental study of cobalt-based alloys designed to contain TiC carbides", Calphad, 2019, 65: 34-41.
https://doi.org/10.1016/j.calphad.2019.02.009

[26] J.-L. Bernard, P. Berthod, L. Héricher, C. Liébaut, S. Michon "Refractory alloy, fiber-forming plate, and method for producing mineral wool", International Patent, PCT Int. Appl, 2009: WO 2009071847 A1 20090611.

[27] P. Berthod, E. Conrath "Mechanical and Chemical Properties at High Temperature of {M-25Cr}-based Alloys Containing Hafnium Carbides (M=Co, Ni or Fe) Creep Behavior and Oxidation at 1200°C" Journal of Material Science and Technology Research, 2014, 1: 7-14.

[28] S. Michon, P. Berthod, L. Aranda, C. Rapin, R. Podor, P. Steinmetz "Application of thermodynamic calculations to study high temperature behavior of TaC-strengthened Co-base superalloys", Calphad, 2003, 27: 289-294.

[29] P. Berthod, Y. Hamini, L. Aranda, L. Héricher "Experimental and thermodynamic study of tantalum-containing iron-based alloys reinforced by carbides : Part I – Case of (Fe,Cr)-based ferritic steels", Calphad, 31: 351-360.

[30] P. Berthod, Mélissa Ritouet-Léglise."Microstructure" and hardness of model niobium-based chromium-rich cast alloys, Advances in Materials Research, 2018, 7(1): 17-28.

BILINGUAL PUBLISHING CO.
Pioneer of Global Academics Since 1984

Journal of Metallic Material Research
https://ojs.bilpublishing.com/index.php/jmmr

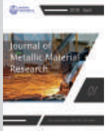

ARTICLE

Hot Cracking Susceptibility of 800H and 825 Nickel-Base Superalloys during Welding via Spot Varestraint Test

Chih-Chun Hsieh[1,*] Ching-Yi Pao[2] Weite Wu[2]

1. Department of Aircraft Engineering, Air Force Institute of Technology, No.1, Julun Rd., Gangshan Dist., Kaohsiung City 820, Taiwan
2. Department of Materials Science and Engineering, National Chung Hsing University, 145 Xingda Rd. Taichung 402, Taiwan

ARTICLE INFO

Article history
Received: 24 February 2019
Accepted: 15 March 2019
Published Online: 19 April 2019

Keywords:
Gas tungsten arc welding
Hot cracking sensitivity
Nickel-base superalloys
Heat-affected zone

ABSTRACT

Hot cracking susceptibility of fillers 52 and 82 in 800H and 825 nickel-base superalloys was discussed using the Spot Varestraint test. The fillers of 52 and 82 were added into nickel-base superalloys via a gas tungsten arc welding (GTAW).Experimental results showed that the hot cracking sensitivity of the nickel-base superalloys with filler at high temperature was lower than that without filler. The hot cracking sensitivity had a slight effect when the filler 82 was added. The total length of crack was increased, the liquid-solid (L-S) two-phase range is higher so that the hot cracking susceptibility will be raised. The morphologies of cracks included the intergranular crack in the molten pool, molten pool of solidification cracking, heat-affected zone of intergranular cracks, and transgranular crack in the heat-affected zone.

1. Introduction

The cracks of the components often been occurred in the aerospace industry under high temperature corrosion and strain environments so that the industrial loss and casualty [1-3]. In the early 1960s, Kammer et al. [4] separated weld cracks into two categories: hot cracking and cold cracking. When cracks occurred near the solidification temperature, they were called hot cracks. Also, Hemsworth et al. [5] classified high-temperature weld cracks for both single-and multipass welds. The two main categories were segregation cracking (including solidification and liquation cracking) and ductility-dip cracking. Other studies have suggested cracks have resulted from high temperatures during reheating in multipass welding, repair welding, or postweld annealing; all of these are known as reheat cracking. Hot cracking in welding applications or experiments appears in stainless steels, Al alloys, superalloys, carbon steels, alloy steels, Ti alloys, and Cu alloys. Hot cracking occurs in the base material's heat-affected zone (HAZ) or in the weld itself. The failure mode is intergranular.

Some harmful secondary phase (Such as: σ phase, μ phase, and Laves phase) can be precipitated in nickel alloys if the chemical composition cannot be controlled during the heat treatment. These precipitate phases can decrease the fracture strength and ductility and then cause the cracks [6-8].

**Corresponding Author:*
Chih-Chun Hsieh,
Department of Aircraft Engineering, Air Force Institute of Technology, No.1, Julun Rd., Gangshan Dist., Kaohsiung City 820, Taiwan;
Email: 1106010@gwolian.com

DOI: https://doi.org/10.30564/jmmr.v2i1.958

In this study, the hot cracking susceptibilityin different nickel alloys of 800H, 825, 800H-52, 800H-82, 825-52, and 825-82 was investigated using the GTAW welding. A series of equipment was used to discuss the crack mechanism, such as the Varestraint test, optical microscope (OM), scanning electron microscope (SEM), X-ray diffractometer (XRD), and differential scanning calorimetry (DSC). The solidus temperature (T_S) and liquidus temperature (T_L) can be measured via the Differential Thermal Analysis and calculate the solidus-liquidus difference value (ΔT). The ΔT index was used to evaluate the hot cracking susceptibility in this study.

2. Experimental Procedures

The 800H and 825 nickel-base superalloys were welded using the gas tungsten arc welding (GTAW). The welding was performed with Nickel filler metals of 82 and 52 and welded on 800H and 825 Nickel alloys. The spot welding was carried out and hot cracking was estimated using the Spot Varestraint machine (see Figure 1). The welded samples were used to observe the microstructures, composition, macrostructures, average amount, average length, and maximum length.

The Incoloy 800H and Incoloy 825 were used for the experimental substrates and specimen size was 200 mm × 50 mm × 5 mm. The Incoloy 82 (#82) and Incoloy 52 (#52) were selected for the filler metals and their diameters were 1.2 mm. The detailed composition was listed in Table 1. The groove types can be divided into the grooved and not grooved specimen. The grooved sample was a single V-Groove with 90° and a distance between an oblique angle and bottom was 1 mm. The same positions were taken for the welded sample with filler and without filler. The top and bottom parts were ground to 1 mm and final sample thickness was 3 mm. The best welding parameters of the filler welding and Spot Varestraint test were determined as shown in Tables 2 and 3.

The relationship between applied strain and crack length were discussed by Varestraint test and evaluate the hot cracking susceptibility [9-11]. The crack in the HAZ and fusion zone (FZ) was estimated using the SOB (Spot on Bead) test [12-16]. The Argon welding gun moved from left to center during test and the mold block of specific curvatureradius is under the sample.

Both ends of the specimen were extruded via an oil pressure arm and then the center points of specimen were bent. Hence, the surface of specimen formed a strain (ε), as indicated as Equation 1:

$$\varepsilon(\%)=t/2/R \quad (1)$$

where ε: The strain in the surface

t: The thickness of specimen

R: The curvature radius of the mold block

The relationship between the amount of crack and the crack length were observed using the Stereo binocular microscope after Spot Varestraint test.

The composition in the matrix and welds was analyzed using the Spark discharge spectrometer. Five measured points were taken in smooth sample surface. Finally, an average value was calculated.

For the Spot Varestraint specimen, the observation regions had three parts of center, solidified zone, HAZ in order to analysis the hot cracking susceptibility. The specimen were divided into 20 portions were observed using the Stereo binocular microscope.

Three observed directions of can be divided into the normal direction (ND), tangential direction (TD), and welding direction (WD) in the welds (see Figure 2), and cut the rolled samples into a suitable size using a precision cutting machine. And then mounted by molding epoxy, then ground using #100~#200 SiC papers and polished with 0.05 μm Al_2O_3 powder paste. The Aqua regia plus Glycerin was used as an etchant for 60 seconds. Finally, the samples of the substrate and welds were observed using the optical microscope (ZEISS Axioskop 2 MAT, OM).

An X-ray diffractometer (Siemens D5000, XRD) with Cu Kα radiation was utilized to analyze the effect of precipitates on hot crack in the substrate and welds at a scanning rate of 2°/min and a 2θ value from 20° to 100°.

The relationship between precipitates of hot crack and filler were discussed using a Field Emission Scanning Electron Microscope (JSM-6700F JEOL, FESEM). The elemental analysis of the TiN or other precipitates were performed by using an Energy Dispersive Spectrometer (EDS).

Hardness of the substrate, HAZ, and welds were measured by a Vickers hardness tester with a 300 g load for 10 seconds at a quarter plane from the specimen surface.

The 800H, 825, 800H-52 (with #52 filler), 800H-82 (with #82 filler), 825-52 (with #52 filler), and 825-82 (with 82 filler)were sampled within 100 mg and analyzed thethermal reactions using the Differential Thermal Analysis (STA PT 1600 Linseis, DTA). The experimental temperature range is between 1273K(1000°C) and 1773K(1500°C) with a heating rate of 275K(2°C)/min. The solidus temperature (T_S), liquidus temperature (T_L), solidus-liquidus coexistent zone(ΔT) can be measured via the DTA. Above indexes can be used to evaluate the hot cracking susceptibility.

DOI: https://doi.org/10.30564/jmmr.v2i1.958

3. Results and Discussion

3.1 Microstructural Observation

Figure 3 showed the metallographic microstructures in the matrixes of the 800H and 825 alloys. Two alloys indicated different equiaxed grains and theirs growth direction had no fixed direction. From the EDS analysis, the inner grains and polygonal particles were identified as the TiN precipitates. The 800H and 825 are the Fe and Ni solution strengthening nickel alloys and had many annealing twins. The microstructures exhibited bigger grains in 800H alloys than that in 825 alloys. Therefore, it showed bigger TiN precipitates in 800H alloys. The cooling time can affect the grain size at the final step of the solution treatment. The grains had enough time to nucleate and grow under a sufficient cooling time. The big size TiN grains will be formed.

Figures 4-6 showed the metallographic microstructures of the ND, TD, and WD of the welds in 800H-52 filler, 800H-82 filler, 825-52 filler, and 825-82 filler, respectively. The results indicated that no TiN precipitate existed in the welds of four nickel alloys. This is because that the high cooling rate leads to high temperature gradient so that the columnar and dendritic structures are formed.

Microstructure development of four alloys fillers (800H-52, 800H-82, 825-52, and 825-82) from a fusion boundary to a center was planar →columnar dendrite → equiaxed dendrite. The difference of these microstructures is from the temperature gradient. The temperature loss in fusion boundary is lower than that in the center so that the microstructure in fusion boundary indicated the planer structure. Furthermore, the cooling rate is higher in the center than that in other regions so that the microstructure showed the equiaxed grains.

3.2 X-ray Diffraction Analysis

Figure 7 showed the XRD results of the welds in 800H, 825, 800H-82, and 825-82 alloys. Results indicated that the Ni-Cr-Fe phase was found in these alloys. This phase was identified as a FCC γ-phase. However, no second phase was examined from diffraction patterns, e.g. $M_{23}C_6$, σ phase, or other low melting point phase. This is because that the grain size of the carbides or other precipitates was small so that XRD cannot detect them.

3.3 Micro hardness Analysis

Figure 8 showed the Vickers hardness on the surface of the 800H, 825, 800H-52, 800H-82, 825-52, and 825-82. The hardness in 800H alloy was lower than that in 825 alloy. The 800H and 825 alloys are the Fe and Ni solution strengthening alloys. In general, two alloys should indicate a similar hardness value. However, the grain size in 825 alloys was smaller than that in 800H alloys from the microstructural observation attributed to an effect of grain refinement strengthening. According to the EDS results, lots of the TiN precipitates were found in the surface of alloys.

3.4 Thermal Analysis

Figure 9 showed the exothermic curves of the 800H, 825, 52 alloy filler, 82 alloy filler, 800H-52, 800H-82, 825-52, and 825-82. The liquidus temperatures (T_L) in 800H, 800H-52, 800H-82, 825, 825-52, 825-82, 52 filler, and 82 filler were 1709K(1436°C), 1676K(1403°C), 1651K(1378°C), 1654K(1381°C), 1671K(1398°C), 1637K(1364°C), 1669K(1396°C), and 1561K(1288°C), respectively. The temperature difference of residual liquid during the solidification can be represented as an index of the ΔT ($T_L - T_S$). The T_L and T_S are the liquidus temperature and solidus temperature. When the value of the ΔT is higher, residual liquid will be kept a long time at high temperature and then lose the strength of grain boundaries during coolingshrinkage. Consequently, the hot cracking will happen. No phase transformation was detected from the thermal analysis and then thesingle stabilizeγ-phase was found in the nickel alloys from the XRD analysis. Table 4 showed the thermal analysis results of the nickel alloys. These ΔT values can be used to predict the hot cracking susceptibility in the nickel alloys. The order of hot cracking susceptibility of the nickel alloys was (a): 800H>800H-52>800H-82; (b): 825-52>825-82>825.

3.5 The Crack Analysis

Fig 10 showed the macrostructure observation of the cracks in 800H, 825, 800H-52, 800H-82, 825-52, and 825-82 alloys. The crack observation was performed using the spot welding via a Spot Varestraint test. The critical strain of experimental samples can be increased rapidly after the spot welding and it can equalize the critical strain and crack strain. Then, the crack will be expanded along the fusion boundary. The distribution of the cracks can be divided into four regions of the center zone (CZ), FZ, partial melted zone (PMZ), and HAZ, as shown in Figure 11. The arc shear stress occurs during the welding and the surface tension exists in the center of the FZ because the center zone is close to the welding gun. The concaveshrinkage can be observed in the center zone and longer and deeper cracks can be formed in this region. However, the dendritic microstructures were found in the FZ. The residual liquids can backfill the cracks during the solidification

DOI: https://doi.org/10.30564/jmmr.v2i1.958

so that this region has no obvious macro-crack. The PMZ is the closest region of the fusion boundary. This region indicated the semi-fused liquid and the poor liquidity and a little residual liquid under high temperature. Consequently, it cannot backfill the cracks in the PMZ.

The cracks can be divided into two parts of (a) dendritic solidification crack in center zone and (b) low ductility crack in HAZ, as shown in Figure 12. The temperature difference of solid and liquid was small during solidification in welding pool and in center zone so that backfill of the residual liquid was not enough. Therefore, the solidification crack can occur during cooling because of shrinkage. The liquation film will be formed in the grain boundary if the low melting point phase precipitates in the dendrite and the HAZ. Hence, the liquation film crack will be occurred. In this study, no low melting point phases at high temperature were detected from the DTA analytical results. The formation mechanism of the cracks should be a low ductility crack. When a liquid is solidified into a solid during the solidification, the low ductility in the HAZ and high strain during thermal expansion and contraction will lead to the intergranular crack.

3.6 The Amounts of Cracks

The average amounts of cracks were shown in Figure 13. The amount measurement of crack can divide into three regions of the center zone, FZ, HAZ plus PMZ (HAZ+PMZ). The crack length of the center zone in 800H alloy was the longest and obvious. However, the crack length of the crack of the center zone in 825-82 alloy was the shortest and unobvious. The order of crack amount in the center zone was 800H>800H-52>800H-82 and 825>825-82>825-52. However, that in the FZ was 800H>800H-52>800H-82 and 825>825-82>825-52. Furthermore, that in the HAZ+PMZ was 800H>800H-52>800H-82 and 825>825-52>825-82. From the amount of cracks and thermal analyses, the results of the crack amount and the ΔT value in the HAZ+PMZ indicated the same tendency. When the ΔT value increases, the amount of cracks will be increased.

3.7 Total Length of the Cracks

Figure 14 showed the total length of the cracks in the nickel alloys of the center zone, PMZ+HAZ, and FZ. The total crack length (TCL) can be used to examine the hot cracking susceptibility. Generally, the amounts of the cracks were higher; the total length of the cracks was longer. The order of total length of the cracks in the center zone was 800H>800H-82>800H-52 and 825-82>825>825-52. On the other hand, that in the FZ was 800H>800H-82>800H-52 and 825-82>825-52>825. Besides, that in the HAZ+PMZ was 800H>800H-52>800H-82 and 825>825-52>825-82. The total length of the crack in 800H alloy was the longest of the all nickel alloys so that the ΔT value was highest in 800H alloy. Consequently, the hot cracking susceptibilityin 800H was more evident.

The crack analyses indicated the same tendency of the hot cracking susceptibility (800H>800H-52>800H-82; 825>825-52>825-82) in the HAZ+PMZ of the all nickel alloys. The hot cracking susceptibility was the highest in the 800H and 825 alloys without filler addition. However, the hot cracking susceptibility can be decreased with filler addition. Because the ΔT value in the 800H alloy was high so that the hot cracking susceptibility was more obvious. Although the ΔT value in the 825 alloys was smaller than that in the 800H alloys, the hot cracking susceptibility in the 825 alloys was higher than that in the containing filler nickel alloys. Above results were because of following two reasons: (a) The grain size in matrix; (2) The dendrite in the surroundings of the welds during welding. For a bigger grain, the intergrain is easy to slip under high temperature strain and then the cracks grow easily, as shown in Figure 15(a). For a smaller grain, the intergrain is difficult to slip under high temperature strain and the growth of the cracks was retarded, as shown in Figure 15(b). However, many dendritic structures in the welds with filler suppressed the mobility of the dendrite arms and then the propagation of the cracks became difficult, as indicated in Figure 15(c). Therefore, the hot cracking susceptibility in the 825 alloys with 52 and 82 fillers can be decreased because of the interaction between dendrite arms.

3.8 Microstructures in the Surface of the Cracks

Figures 16-17 showed the microstructural distribution of the Varestraint test. Figures 16(a) and 17(a) were microstructures of the HAZ and had some annealing twins and smaller black points of the TiN precipitates in the grained structures. However, the microstructures indicated a planar growth if the filler was added into the matrix. Figures 16(b) and 17(b) were microstructures of the partial melted zone (PMZ) and the microstructures were similar to the FZ. This region was a like-planar growth and every planewas different direction growths. Figures 16(c) and 17(c) showed the microstructures of the FZ and this region exhibited a dendritic growth. It closed to the center area and had an obvious temperature gradient so that the dendritic growth was observed. Figures 16(d) and 17(d) were microstructures of the center zone and the microstructures were the equiaxed structures under high temperature difference.

DOI: https://doi.org/10.30564/jmmr.v2i1.958

Figure 18 showed the metallographic observation of the crack in the nickel alloys and Figure 19 indicated the schematic diagram of different crack modes. Figure 19(a) was a crack in the FZ and high temperature difference led to the dendritic growth. The residual liquid does not backfill the crack completely so that the crack expanded along the two sides of dendrites. The residual liquid will be concentrate on the dendrites. Hence, the cracks were formed in above region under a critical deformation of the Varestraint test. Figure 19(b) showed the transgranular crack in the HAZ. The matrix without filler addition was located in this region. It does not form a weak region for residual liquid in the dendrites and grains so that the transgranular crack can be occurred directly. Figure 19(c) was a crack with filler addition and the cracks were expanded in this area along the dendritic boundaries. The boundaries of different directions were weak so that the dendritic boundaries were beneficial region to form the cracks. Figure 19(d) exhibited the cracks for a planar growth in the partial FZ. The orientation in the partial zones was very random and the strength in the grains was low so that the cracks were formed easily along the grain boundaries.

Figure 20 showed the SEI and BEI micrographsin the starting and terminal points of the cracks of 800H-52 alloys. The observed result is the same as Figure 19(d) and the starting point of the crack was formed along the grain boundaries of different directions. The terminal point of the crack was similar to the Figure 19(b). No residual liquid can expand the cracks so the growth mode of crack was a transgranular crack. The compositional results were indicated in Table 5. Figure 20(a) indicated that the composition in the starting point issimilar to that in the grains. Furthermore, lots of the TiN precipitates in the cracks of the terminal point HAZ. Figure 20(b) showed that the BEI micrograph for a starting point and a terminal point of the cracks. There were no harmful precipitates for cracks in the starting point and terminal point. Hence, the formation of the cracks had no relationship with the Al phase, Ti phase, B phase, P phase, S phase, γ' phase, Laves phase, and carbide whether fillers addition or not 800H and 825.

4. Conclusions

(1) The order of hot cracking susceptibility in nickel-basesuperalloys of 800H and 825during welding was 800H>800H-52>800H-82 and 825>825-52>825-82, respectively. The hot cracking susceptibility in the 825-82 alloy was the poorest of the all nickel alloys.

(2) When the 52 and the 82 fillers were added into the 800H and 825 alloys, the ΔT value will be decreased. The order of theΔT value in nickel alloys was 800H>800H-52>800H-82 and825-52>825-82>825, respectively.

(3) The solidification crack expanded along the grain boundaries or orientation grains and the growth mode of crack is the transgranular crack in the HAZ.

Acknowledgements

The authors are obligated to thank the Ministry and Science and Technology (MOST) of the Taiwan, R.O.C. for the financial support under the projects numbered MOST 103-2218-E-005-002.

Supplements

Table 2. Welding parameters of filler welding

Torch speed	120mm/min
Voltage	14V
Current	180A
Wire speed	193cm/min

Table 3. Welding parameters of Spot Varestraint test

Voltage	17.6V
Current	122A
Augmented Straint Range	5%
Under the push interval	0.1s
Welding time	3s

Table 4. Thermal analysis results of nickel alloys

	T_L(degree)	T_S(degree)	ΔT(degree)
800H	1436.4	1414.9	21.5
825	1381.0	1377.7	3.3
Filler 82	1288.1	1284.6	3.5
Filler 52	1396.4	1392.3	4.1

Table 1. Chemical composition of experimental materials

	Ni	C	Fe	Cr	Cu	Mo	Co	W	Mn	Al	Nb	Ti	Si
800H	31.24	0.102	45.94	19.89	0.020	0.304	0.023	0.642	1.07	0.447	0.093	0.385	0.177
825	40.19	0.025	31.51	20.80	2.775	3.442	0.000	0.102	0.583	0.090	0.118	0.526	0.204
#82	73.40	0.05	0.61	19.95	-	-	-	-	2.88	-	-	0.40	0.09
#52	58.50	0.03	9.60	28.90	-	-	-	-	0.26	0.57	-	0.55	0.24

DOI: https://doi.org/10.30564/jmmr.v2i1.958

800H-52	1402.8	1399.6	3.2
800H-82	1377.9	1375.1	2.8
825-52	1397.7	1390.9	6.8
825-82	1363.9	1359.5	4.4

Table 5. EDS analysis of surrounding the cracks

Point	**Element (wt%)**				
	Cr	Fe	Ni	Ti	N
a	24.42	28.33	47.25	-	-
b	24.34	26.91	48.76	-	-
c	12.36	44.11	44.09	-	-
d	-	-	-	36.53	63.47

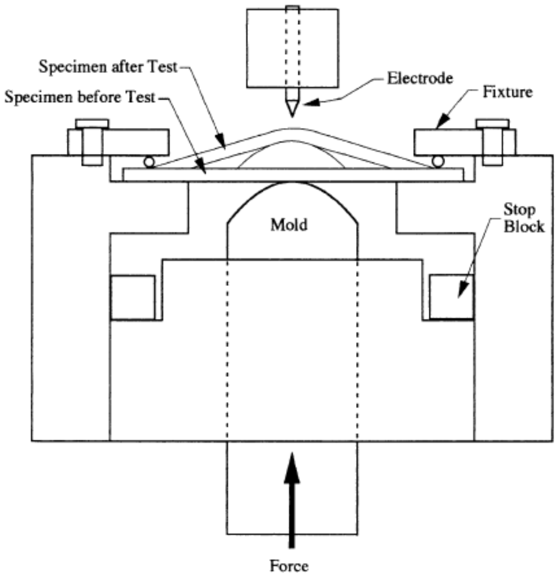

Figure 1. Spot Varestraint test apparatus

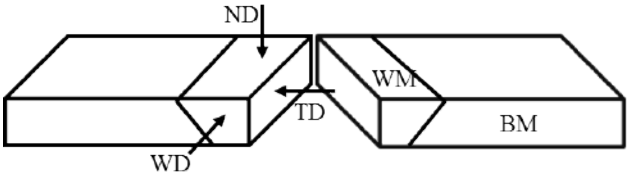

Figure 2. Definition of regions for microstructural observation

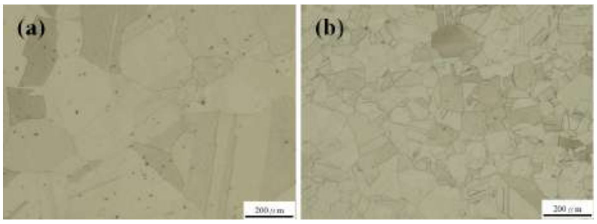

Figure 3. Metallographic microstructures of nickel-base-superalloys

Note: (a) 800H (b) 825 with an etchant of the Aqua regia plus Glycerin

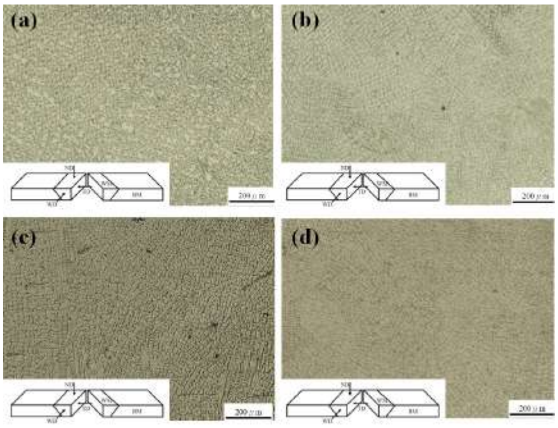

Figure 4. Microstructures of nickel-basesuperalloys in normal direction (ND)

Note: (a) 800H-52 (b) 800H-82 (c) 825-52 (d) 825-82 with an etchant of the Aqua regia plus Glyce

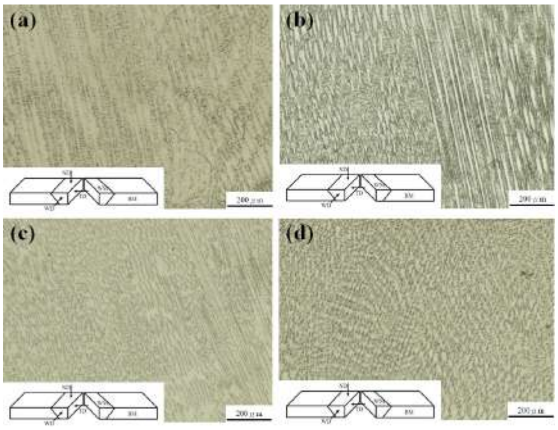

Figure 5. Microstructures of nickel-basesuperalloys in tangent direction (TD)

Note: (a) 800H-52 (b) 800H-82 (c) 825-52 (d) 825-82 with an etchant of the Aqua regia plus Glycerin

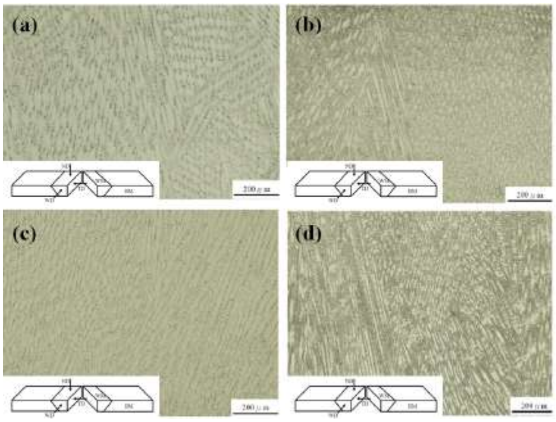

Figure 6. Microstructures of nickel-basesuperalloys in welding direction (WD)

Note: (a) 800H-52 (b) 800H-82 (c) 825-52 (d) 825-82 with an etchant of the Aqua regia plus Glycerin

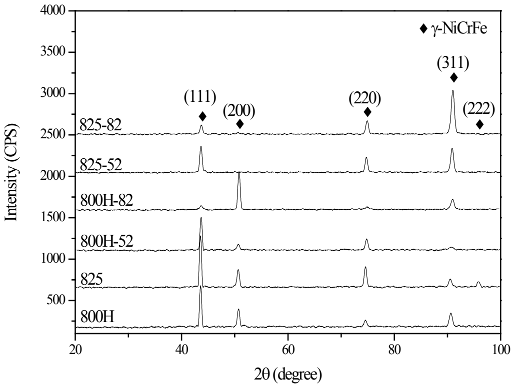

Figure 7. XRD diffraction pattern of nickel-base superalloys

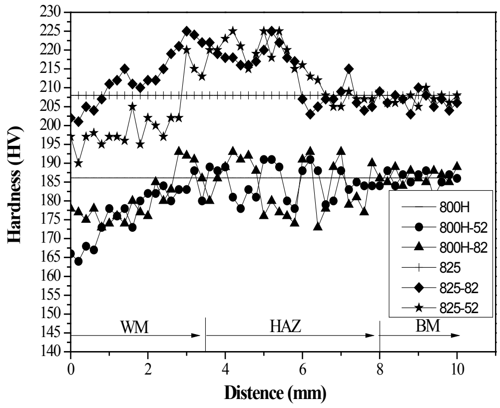

Figure 8. Vickers hardness of nickel-basesuperalloys

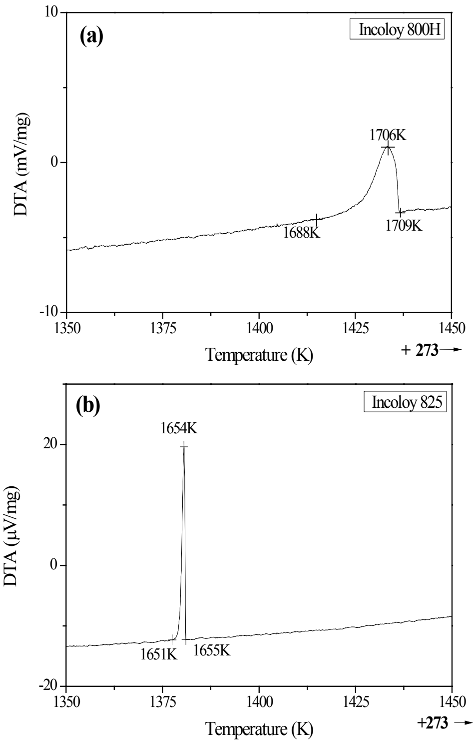

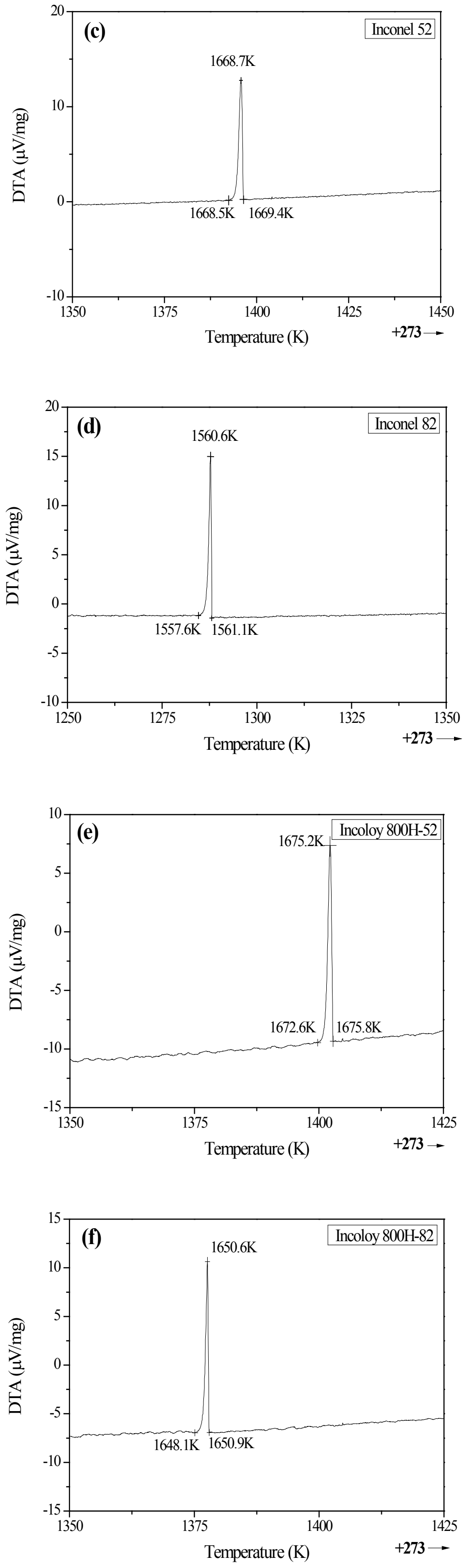

DOI: https://doi.org/10.30564/jmmr.v2i1.958

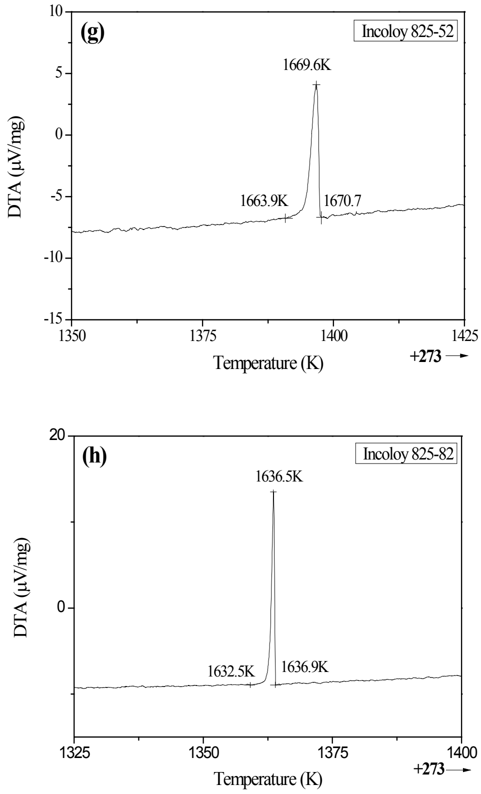

Figure 9. DTA thermal analysis of nickel-basesuperalloys

Note: (a) 800H (b) 825 (c) 52 filler (d) 82 filler (e) 800H-52 (f) 800H-82 (g) 825-52 (f) 825-82

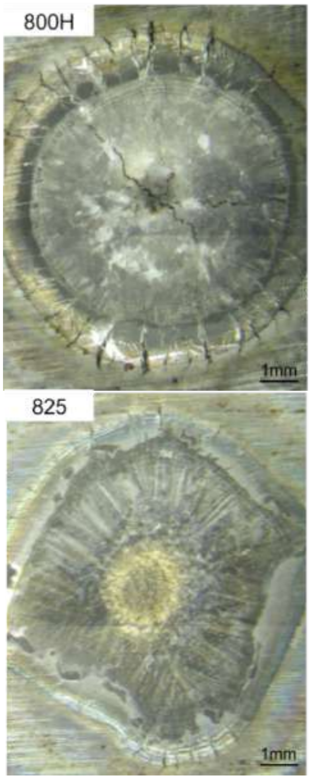

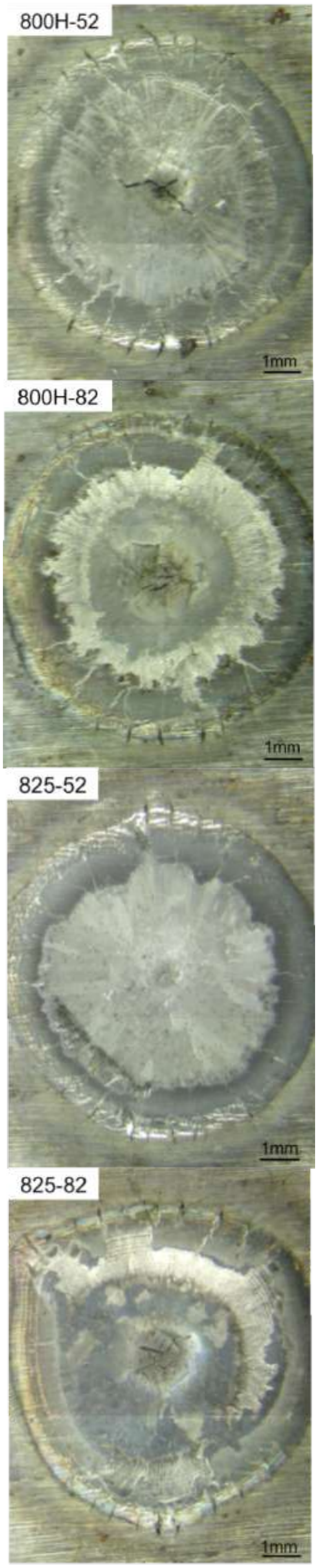

Figure 10. Macrostructures of cracks after Spot Varestraint test

DOI: https://doi.org/10.30564/jmmr.v2i1.958

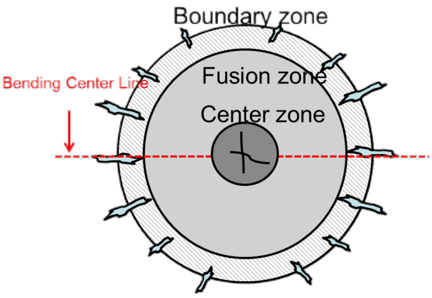

Figure 11. Schematic diagram showing the welding zones after Spot Varestraint test

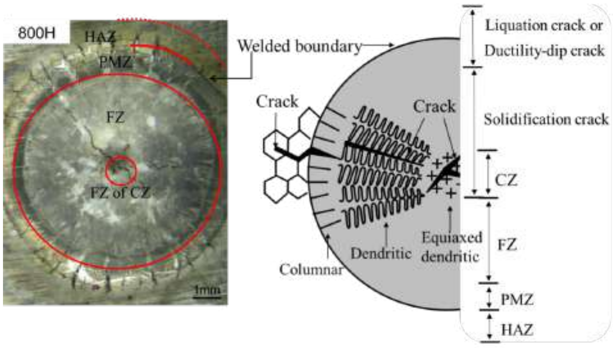

Figure 12. Schematic diagram showing the crack growth and crack mode in nickel-base superalloys

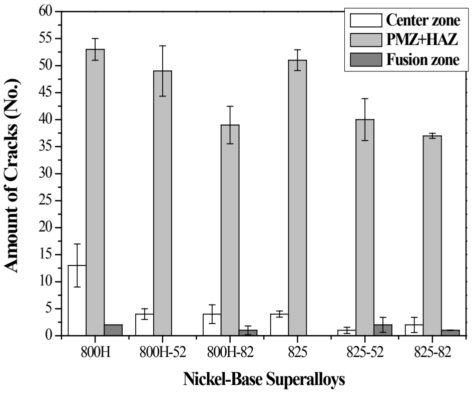

Figure 13. Amount of cracks in nickel-base superalloys

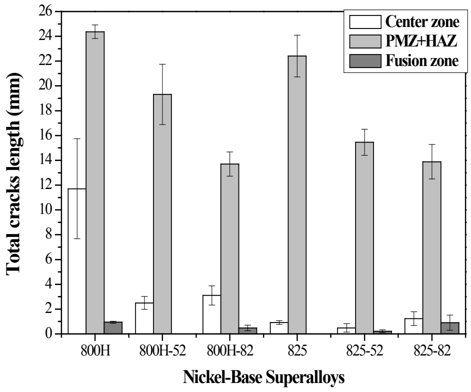

Figure 14. Total cracks length in nickel-base superalloys

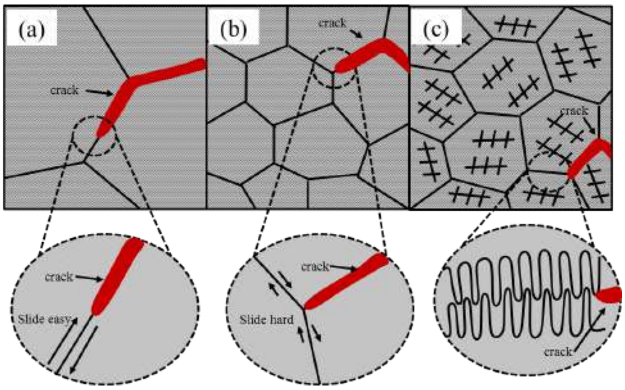

Figure 15. Microstructural development of cracks in nickel-base superalloys

(a)

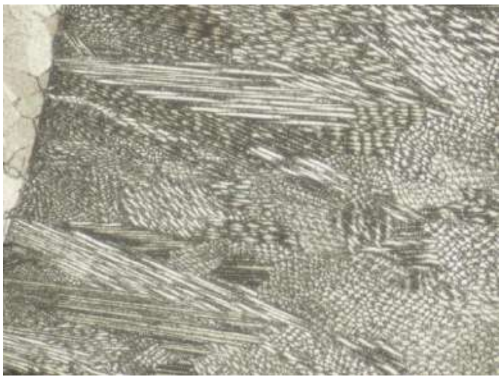

(b)

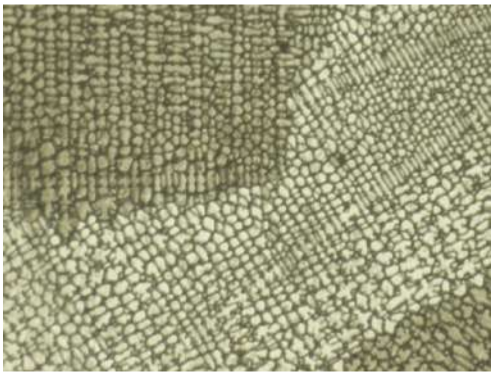

(c)

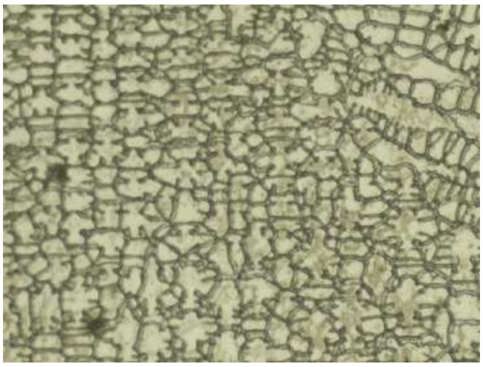

(d)

Figure 16. Microstructures of Spot Varestraint test in different regions

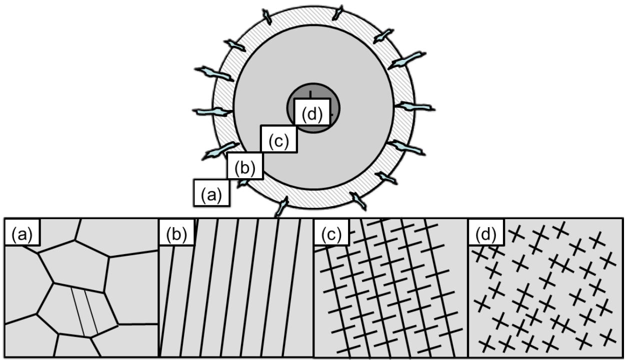

Figure 17. Schematic diagram showing the microstructures in different regions after Spot Varestraint test

(a)

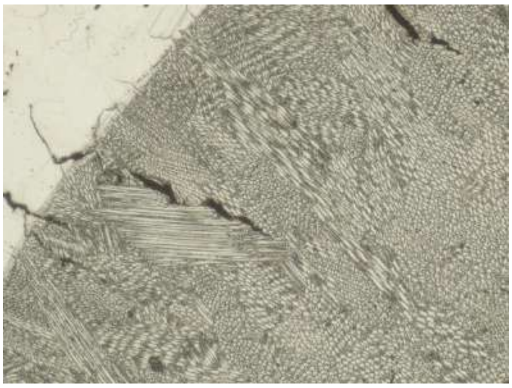

(b)

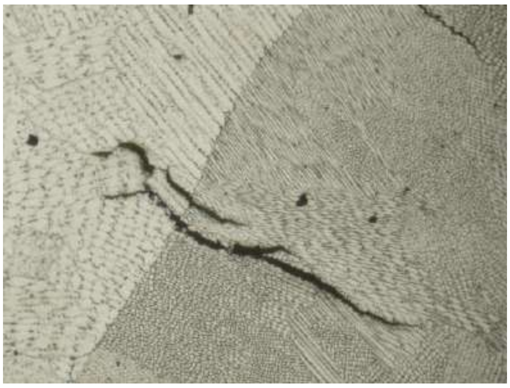

(c)

(d)

(e)

DOI: https://doi.org/10.30564/jmmr.v2i1.958

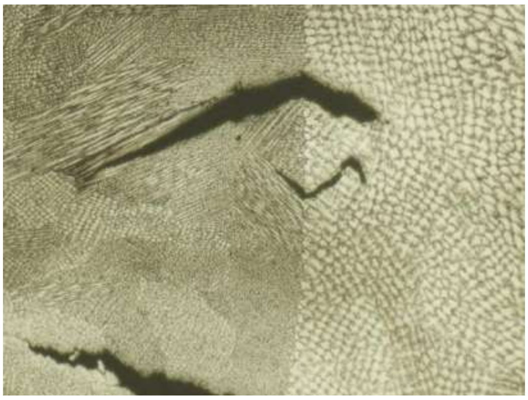

(f)

Figure 18. Metallographic micrographs of cracks in nickel-base superalloys

Note: (a) 800H, (b) 825, (c) 800H-52, (d) 825-52, (e) 800H-82, (f) 825-82

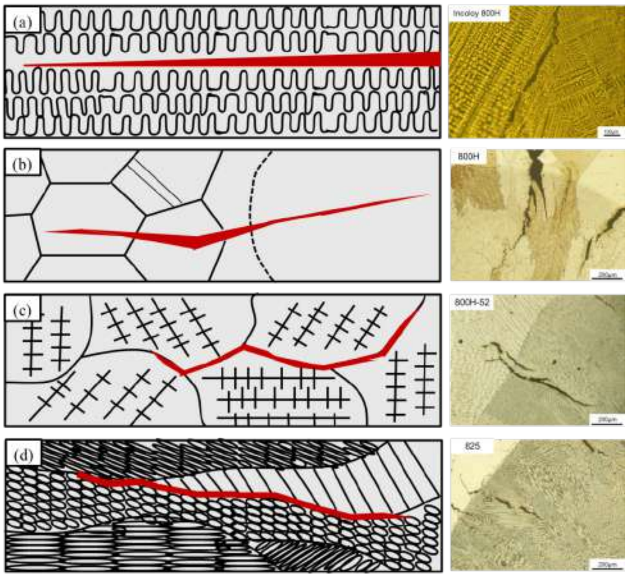

Figure. 19 Different growth modes of cracks in different nickel-base superalloys

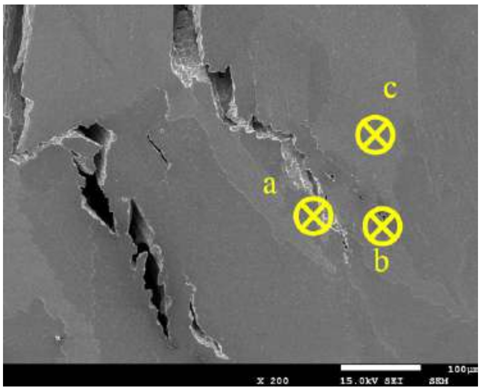

(a)

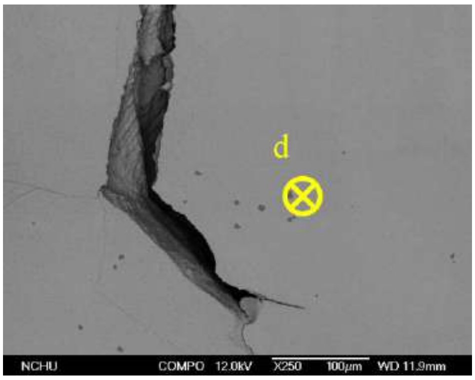

(b)

Figure 20. SEM micrographs in surrounding cracks (a) starting point, (b) terminal point

References

[1] R.A. Page: Corrosion, 1983, 39(21): 409.

[2] R.A. Page and A. McMinn: EPRI NP-5882M Project 1566-1 Final Report, 1988.

[3] H.C. Burghard and A.J. Bursle: SWRI Project 02-5839-001 Final Report, 1978.

[4] P.A. Kammer, K. Masubuchi, and R.E. Monroe: Defense Metals Information Center, DMIC Report 197, 1964.

[5] B. Hemsworth, T. Boniszewski, and N.F. Eation: Metal Const. Br. Weld. J., 1969, 2: 5-16.

[6] X. Ye, X.M. Hua, Y.X. Wu, and S.N. Lou: J Mater. Process Technol., 2015, 217: 13-20.

[7] C. Bellot and P. Lamesle: J. Alloy Compd., 2013, 570: 100-03.

[8] N.R. Sun, L.T. Zhang, Z.G. Li, and A.D. Shan: Mater. Sci. Eng. A, 2014, 606: 417-25.

[9] Y.N. Li, X.S. Liu, J.C. Yang, M. Lin, L. C.F. Li: Mater. Design, 2012, 35: 303-09.

[10] J. Zhang: Scripta Mater., 2003, 48(81): 677.

[11] Y.P. Mei, Y.C. Liu, C.X. Liu, C. Li, L.M. Yu, Q.Y. Guo, and H.J. Li: Mater. Design, 2016, 89(77): 964.

[12] M.T. Rush, P.A. Colegrove, Z. Zhang, and B. Courtot: Adv. Mater. Res., 2010, 89-91(72): 467.

[13] C.P. Chou and C.H. Chao: REPAIR WELDABILITY STUDIES OF ALLOY 718 USING VERSATILE VARESTRAINT TEST, Superalloys, The Metallurgy Society, 1988(93): 785.

[14] C.M. Cheng, C.P. Chou, I.K. Lee, and I.C.Kuo: J. Mater. Sci. Technol., 2006, 22: 685-690.

[15] C.C. Chang, C.L. Chen, J.Y. Wen, C.M. Cheng, and C.P. Chou:Mater. Manuf. Process, 2012, 27(63): 658.

[16] W. Wu and C.H. Tsai: Metall. Mater. Trans. A, 1999, 30(26): 417.

DOI: https://doi.org/10.30564/jmmr.v2i1.958

BILINGUAL PUBLISHING CO.
Pioneer of Global Academics Since 1984

Journal of Metallic Material Research
https://ojs.bilpublishing.com/index.php/jmmr

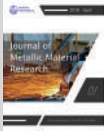

ARTICLE

Lateral Dispersion Pattern of Main Indicators at the Glojeh Polymetallic Deposit, NW Iran

Farshad Darabi-Golestan* **Ardeshir Hezarkhani**

Department of Mining and Metallurgical Engineering, Amirkabir University of Technology. 424 Hafez Ave, Tehran, Iran

ARTICLE INFO

Article history
Received: 8 March 2019
Accepted: 22 March 2019
Published Online: 19 April 2019

Keywords:
Iterative stepwise regression
Interaction effects
Lateral zonation
Linear productivity
Kriging technique

ABSTRACT

The criterion-base iterative stepwise Backward Elimination (BE) method was used to predict Au according to the main variables (Ag, Cu, Pb, and Zn). The optimization process of the quadratic polynomial model are carried out on different trenches. Whereas, Pb and Zn with Ag×Zn and Pb×Zn are significant to determine the lateral dispersion of Au. It means Zn is the predominant element in near surface zone. Therefore, it point out that the polymetallic (Au-Ag-Cu-Pb-Zn) high-sulfidation hydrothermal veins may be related to a porphyry deposit at depth. Laterally, 2D surface contour maps using kriging confirms all the results of the dispersion pattern of elements at Glojeh.

1. Introduction

Different geochemical interaction processes occur between the host rock and vein in the Glojeh polymetallic deposit. By consideration of the variables interaction effects (IE) can improve the accuracy of processing or modeling [1-5]. Hence, the quadratic terms (X^2) and the first order interaction (Xi×Xj) of variables were constructed with the aim of examining the relationship between geochemical variables. Stepwise regression analysis (RA) and analysis of variance (ANOVA) can be applied to determine the interactions between elements [6, 7], the dispersion pattern and elemental associations in mineralization using some geochemical concepts. Backward Elimination (BE) is one of the Stepwise Regression methods. Stepwise regression serves to reduce the model by using the strategy to eliminate the predictors which do not contribute to model accuracy, according to reach the specific accuracy.The quadratic polynomial model (QPM) considered as a full model to elucidate the relationship between variables. BE procedure is just a one procedure within the Stepwise regression where the starting model is actually a full model (model with all possible predictors) and then algorithm sequentially removes the worst one predictor while its accuracy is improving according to one criteria. Accordingly, some criteria including different criteria (R^2, R^2 adjusted[adj.], R^2 predicted[pred.]), PRESS, and F-ratio were used more frequently [5, 8, 9]. The BE modeling applied according to p-values (or laterally t-test) and related confidence levels [10, 11]. The convergent trend of R^2, R^2(adj.), R^2(pred.) accompanied by increases

---

**Corresponding Author:*
Farshad Darabi-Golestan,
Department of Mining and Metallurgical Engineering, Amirkabir University of Technology. 424 Hafez Ave, Tehran, Iran;
Email: pooyan@aut.ac.ir

DOI: https://doi.org/10.30564/jmmr.v2i1.1001

of F-value, and decreases of PRESS (Prediction Error Sum of Squares) indicate more accurate optimization [12]. The model with the lowest PRESS may be desirable, if the prediction is the objective of using this method.All the parameter and variables contributed at the full model with the lowest significant (p-value and t-value). According step by step process of elimination of parameters the model accuracy have been optimized. Besides, the full model has the lowest criteria for prediction (R^2(pred.)) new observation. During elimination of insignificant predictors the model is optimized gradually.

In this study, the authors have tried to estimate and identify the Au dispersion by associated elements for all trench samples in veins and host rock. The research was conducted with three aims: (a) to recognize the horizontal relationship between variables, statistically and spatially (b) determine an indicator model, (c) and decrease the cost of Au analysis. The relationship between variables is conducted based on examination of drillholes and trenches to determine zonality in polymetallic veins, shear zones, and host rocks, while the results have been validated according to R^2(pred.). The approach is furnished by the BE procedure on iterative RA and ANOVA by definition of IE of elements to improve the overall performance of zonal modeling. Based on BE, gradually all the insignificant predictors were eliminated. Therefore, all the predictors with different presence (the main elements (Xi),quadratic terms (X^2), and the first order interaction (Xi×Xj)) may be related to the object element (it is Au at here). Au variation and dispersion is investigated by first and second order and interactions of other elements which are benefit to determine the elemental zoning sequence.

2. Geological Setting

The Glojeh district is located in the central part of the Tarom- Hashtjin Metallogenic Province (THMP), which is one of Iran's major metallogenic provinces. Structurally, this subduction-related continental margin arc extends from a merging between the western Alborz magmatic belt and Urmieh-Dokhtar zone [13]. The rocks along the THMP are considered equivalent to the Karaj formation. They are different from those in central Alborz in terms of the lithology and chemical composition because the lava flows do not consist only of volcani-clastic rocks along this axis, and their compositions are more basic [14, 15]. Many intrusive bodies in the area have been injected into Eocene volcani-clastic assemblages, so these bodies are post-Eocene (most likely Oligocene) in age. One characteristic of the Oligocene intrusive bodies is the creation of alteration areoles in Eocene volcani-clastics, and a lot of epithermal Au-Cu-Pb-Zn mineralization have been generally occurred due to hydrothermal reactions [14, 16]. The Glojeh district is mainly covered by rhyodacite, lithic tuff, and andesite basalts [17].

3. Materials and Methods

3.1 Exploration Drilling

Tuff, rhyolite, and andesite, tuff- rhyolite and rhyodacite, tuff-rhyolite, and rhyodacite to latite are the host rocks of the TR1, TR2, and TR3, respectively, while TR4, TR5, and TR6 were excavated in rhyodacite to latite rocks. The sample numbers of trenches TR7 and TR8 are only 8 and 6 samples, respectively (Table 1). It is not enough to modeling and they were examined for 2D surface contour maps.The trenches TR4 and TR5 were excavated in rhyolite to rhyodacite with interbedded tuff and ignimbrite and have been covered by silicified alteration (Figure 1 and Table 1).

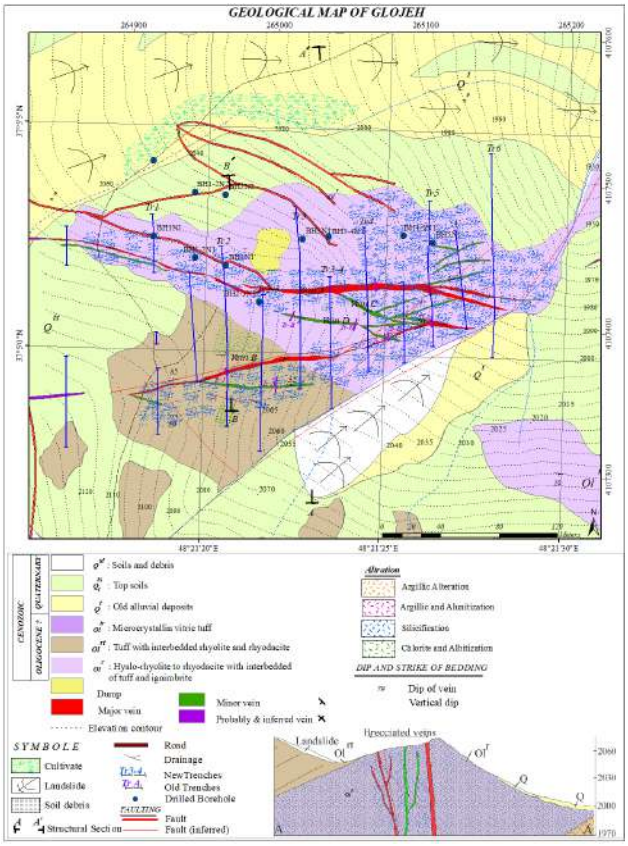

Figure 1. Location and geological map of the Glojeh deposit, including the main trenches

3.2 Backward Elimination

The interaction effect (IE; e.g. X^2 and Xi×Xj) of variables (Ag, Cu, Pb, and Zn) were defined considering different interaction processes between meteoric water and mag-

Table 1. Specifications of the trenches from TR0 to TR8 (ppb was used for all the concentration measurements)

Trench	Length	Alteration	Host rock	Samples	Vein samples	Average Au concentration	Maximum Au concentration	Minimum Au concentration
TR0	96	-	Rhyodacite to latite	43	3	103.9	2980	2.1
TR1	155	Hematite- Limonite	Tuff and Rhyodacite	39	13	1080	6760	3.2
TR2	136	Silicic, Hematite+Argillic	Tuff, Rhyolite, Rhyodacite	62	5	568	4370	4.2
TR3	130	Silicic, Hematite+Argillic	Tuff, Rhyolite, Rhyodacite to latite	60	23	1570	12900	4.9
TR4	103	Silicic, Hematite	Rhyodacite to latite	71	20	2180	21400	30
TR5	103	Silicic, Hematite+Argillic	Rhyodacite to latite	76	38	2275	19450	27
TR6	155	Silicic, Limonitic	Rhyodacite to latite	36	10	480	3540	4.5
TR7	15	Silicic	Rhyodacite	8	1	507.6	3440	34
TR8	14.5	Silicic And week Argillic	Tuff	6	1	141.7	730	8.4

matic fluids as well as host rock and vein in the polymetallic Glojeh deposit. These mathematical interaction revealed by geochemical properties of elements in different lithology and level of mineralization, considering to the level of definition of interaction effects. Therefore, IE play an important role for geochemical exploration and mineral deposition studies, especially in polymetallic hydrothermal ore deposits [18, 19]. Raudenbush and Liu [1], Diggle [2] and Leon and Heo [3] have argued for the use of main and IE of variables in their studies, which lead to improve the accuracy of processing or modeling. In this study, RA and ANOVA were done within BE process. The QPM that is constructed in the first step of BE modeling is given by:

$$Y = \alpha_1 X_1 + \ldots + \alpha_{r-1} X_{r-1} + \beta_1 X^2_1 + \ldots + \beta_{r-1} X^2_{r-1} + \chi_1 X_1 X_2 + \ldots + \chi_n X_{r-1} X_r + \varepsilon \tag{1}$$

where α, β and χ are the coefficients, and X_r is variable. The modeling is restricted to the main effects (variable X_i; Ag, Cu, Pb, and Zn), quadratic terms (covariates X_i^2; Ag^2, Cu^2, Pb^2, Zn^2), and the first order interaction (covariates $X_i \times X_j$; Ag×Cu, Ag×Pb, Ag×Zn, Cu×Pb, Cu×Zn, Pb×Zn) of variables [20]. The coefficient, standard error (SE), t-value ($^{\text{coeficient}}\!/_{\text{SE}}$), and p-value (indicate significance of all variables and covariates) associated with each predictor that contribute in the model were calculated from RA [21, 22]. Accordingly, at RA the parameter R^2 indicates how well the model fits the data and tends to increase as additional predictors added in the model. In order to overcome this effect, the parameter R^2(adj.) which could compare the two linear models with their complexity is utilized. R^2(pred.) was used with ease to compare how well the two model predicts responses for new observations that were not included in model estimation based on leave-one-out cross validation [23, 24].

The ANOVA analysis parameters are shown in Table 2. The F-ratio and R^2 can be obtained as follows (n is equal to the total number of observations in the analysis):

$$F - ratio = {}^{SSR/p}\!\big/_{SSE/(n-p-1)} = {}^{MSR}\!\big/_{MSE} \tag{2}$$

$$R^2 = \frac{SSR}{SST} \tag{3}$$

Table 2. The ANOVA analysis parameters

Source of Variation	Sum of Squares (SS)	Degrees of freedom (df)	Mean Squares (MS)	F ratio
Regression	SSR	p	MSR	MSR/MSE
Error	SSE	(n-p-1)	MSE	
Total	SST	(n-1)		

4. Results: Trenches Investigation

Overall, 401 trench samples were included in this study. They were collected from trench TR0 to TR8 where totally 907.5 meters were excavated. The BE approach has been applied on TR2 and explained in detail. At the first step, the QPM was set to be:

$$\begin{aligned} Au = {} & 1.13 - 0.87\,Ag + 0.29\,Cu - 0.38\,Pb + 1.35\,Zn \\ & -0.12\,Ag \times Cu + 0.44\,Ag \times Pb - 0.50\,Ag \times Zn + 0.47\,Cu \\ & \times Pb + 0.26\,Cu \times Zn - 0.289\,Pb \times Zn + 0.25\,Ag^2 - 0.319\,Cu^2 \\ & -0.252\,Pb^2 + 0.128\,Zn^2 \end{aligned} \tag{4}$$

Accordingly, all the t-test values (accompanied with p-values) of predictors (14 ones) were calculated to determine significant and insignificant predictors. The results of RA and ANOVA are summarized in the Table 3 for different steps and insignificant predictors are determined according to highest p-values. The Ag×Cu and

DOI: https://doi.org/10.30564/jmmr.v2i1.1001

Pb (p-values equal to 0.952 and 0.861, respectively) are removed at the 1st step, because the majority of prediction error that causes uncertainty in the model has been related to these predictors. The eliminating process (BE) was carried out by removing the least useful variables according to partial F ratio, R^2, R^2(adj.), and R^2(pred.) criteria. The R^2 and R^2(pred.) in this step equal 85.50 % and 15.36 %, respectively. When there is a high R^2, while the R^2(pred.) is low, it indicates that the model cannot give very good performance for predicting new observations. This implies that a lot of predictors create huge errors in modeling. Therefore, the model must be optimized by removing the special predictors that create the highest error (Ag×Cu and Pb at first step; Table 3 and Figure 2). At the second step, a new model is generated, while Ag×Cu and Pb have been deleted, and R^2(pred.) increased to 48.08% when R^2 has no significant changes (Figure 2 and Figure 3). An increase of R^2(pred.) accompanied by partial F-test value indicates improvement in the modeling [25]. Subsequently, Cu, Cu×Zn, Ag×Pb, Ag×Zn, Pb^2, Zn^2, threshold value, Cu^2, Ag, and Ag^2 were eliminated, and Reduced QPM (RQPM) was constructed with three predictors (df

Table 3. Regression analyses and ANOVA for BMA of TR2 in Glojeh deposit

step	criteria	value	Source	DF	SS	MS	F	P	Predictor	P-value
1	S	0.515	Regression	14	23.467	1.676	6.33	0.001	Ag×Cu	0.952
	R^2	85.50%	Residual Error	15	3.972	0.265			Pb	0.861
	R^2(adj.)	72.00%	Total	29	27.438					
	PRESS	23.224								
	R^2(pred.)	15.36%								
2	S	0.484	Regression	12	23.458	1.955	8.35	0	Cu	0.885
	R^2	85.50%	Residual Error	17	3.981	0.234			Cu×Zn	0.746
	R^2(adj.)	75.30%	Total	29	27.438					
	PRESS	14.246								
	R^2(pred.)	48.08%								
3	S	0.459	Regression	10	23.427	2.343	11.1	0	Ag×Pb	0.868
	R^2	85.40%	Residual Error	19	4.011	0.211			Ag×Zn	0.719
	R^2(adj.)	77.70%	Total	29	27.438					
	PRESS	11.659								
	R^2(pred.)	57.51%								
4	S	0.439	Regression	8	23.399	2.925	15.21	0	Pb^2	0.69
	R^2	85.30%	Residual Error	21	4.040	0.192			Zn^2	0.54
	R^2(adj.)	79.70%	Total	29	27.438					
	PRESS	9.035								
	R^2(pred.)	67.07%								
5	S	0.428	Regression	6	23.220	3.870	21.1	0	Constant	0.199
	R^2	84.60%	Residual Error	23	4.218	0.183			Cu^2	0.155
	R^2(adj.)	80.60%	Total	29	27.438					
	PRESS	7.933								
	R^2(pred.)	71.09%								
6	S	0.450	Regression	5	389.874	77.975	384.45	0	Ag	0.724
	PRESS	7.033	Residual Error	25	5.071	0.203			Ag^2	0.894
			Total	30	394.945					
7	S	0.435	Regression	3	389.84	129.95	687.29	0	Pb×Zn	0.001
	PRESS	6.062	Residual Error	27	5.1	0.19				
			Total	30	394.94					
8	S	0.528	Regression	2	387.13	193.56	693.13	0		
	PRESS	9.051	Residual Error	28	7.82	0.28				
			Total	30	394.94					

equals to 3 at the 7th step) for 30 samples (total df). It is noteworthy that the $R^2$is reduced a little from 85.5% at QPM to 84.6% at RQPM. It could reveal that R^2 is not an appropriate criterion to improve modeling performance, individually. In the 8th step, it is clear that if Pb×Zn is eliminated, the PRESS and S criteria increase and it is not in order to model optimization. The removal of insignificant predictors cause changes in the t-values of other predictors. Therefore, at TR2, the Zn, Cu×Pb and Pb×Zn predictors with t-values equal to 10.27, 4.53, and 3.79 are the most important predictors for Au modeling (Table 3 on 7th step, Table 4). An improvement in modeling was achieved according to convergent trends through seven steps for R^2, R^2(adj.), and R^2(pred.) accompanied by increases in R^2(pred.) [26, 27]. After the 6th step due to elimination of the threshold value MINITAB software unable to calculateR^2(adj.) and R^2(pred.), therefore the decrease in PRESS and increase in F value indicate the improvement in modeling (Table 4, Figure 2). Finally, through BE procedure the R^2(pred.) is increased from 15.36% in QPM to 71.09% in RQPM, which indicates the ability to predict Au for new samples. It was satisfied only by the genetic relationship between Ag, Cu, Pb, and Zn elements, since many factors are involved in mineralization. The RQPM for TR2 was introduced by the following equation:

$$Au = Zn + 0.181\, Cu\times Pb - 0.183\, Pb\times Zn \qquad (5)$$

According to the significant predictors that contributed in RQPM for TR1, TR2, TR3, and TR6, Pb and Zn were the main predictors, and Pb×Zn was the significant interaction for Au modeling. In these trenches, Ag and the threshold value unusually show high dependency with each other in the process of elimination (Table 4), because the threshold value at step 5 has the largest p-value equal 0.199 but when it was eliminated the p-value of Ag and Ag^2 show sudden increases.

Table 4. The order of elimination insignificant predictors using BE stepwise regression to create RQPM for each trenches

	TR1			TR2			TR3		
	Predictor	P-value	t-value	Predictor	P-value	t-value	Predictor	P-value	t-value
insignificant predictors that eliminated by several optimization steps	Ag	0.963		Ag×Cu	0.952		Constant	0.909	
	Pb×Zn	0.91		Pb	0.861		Ag	0.863	
	Constant	0.837		Cu	0.885		Ag×Pb	0.747	
	Cu×Zn	0.883		Cu×Zn	0.746		Cu^2	0.681	
	Cu	0.472		Ag×Pb	0.868		Cu×Pb	0.502	
	Ag^2	0.441		Ag×Zn	0.719		Zn^2	0.548	
	Ag×Cu	0.658		Pb^2	0.69		Cu	0.336	
	Ag×Pb	0.551		Zn^2	0.54		Cu×Zn	0.416	
	Pb^2	0.853		Constant	0.199		Pb^2	0	4.38
	Zn^2	0.663		Cu^2	0.155		Pb	0	4.28
	Zn	0.17		Ag	0.724		Pb×Zn	0.002	3.34
significant predictors that contributed in RQPM	Pb	0	9.39	Ag^2	0.894		Ag^2	0.005	2.9
	Ag×Zn	0.003	3.18	Zn	0	10.27	Ag×Cu	0.034	2.17
	Cu×Pb	0	4.43	Cu×Pb	0	4.53	Zn	0.052	1.99
	Cu^2	0	4.03	Pb×Zn	0.001	3.79	Ag×Zn	0.113	1.61
	TR4			TR5			TR6		
	Predictor	P-value	t-value	Predictor	P-value	t-value	Predictor	P-value	t-value
insignificant predictors that eliminated by several optimization steps	Ag^2	0.518		Ag×Pb	0.856		Zn	0.998	
	Pb^2	0.568		Ag^2	0.889		Pb^2	0.938	
	Cu	0.001	3.79	Ag	0.836		Ag×Zn	0.92	
	Pb	0.001	3.59	Pb^2	0.885		Ag×Pb	0.807	
	Ag	0.007	2.86	Ag×Cu	0.862		Ag^2	0.874	

DOI: https://doi.org/10.30564/jmmr.v2i1.1001

significant predictors that contributed in RQPM	Ag×Zn	0.009	2.79	Zn	0.49		Cu×Zn	0.824	
	Ag×Pb	0.017	2.52	Pb	0.43		Cu×Pb	0.756	
	Zn	0.014	2.6	Cu	0.28		Cu	0.608	
	Pb×Zn	0.023	2.38	Cu^2	0.395		Constant	0.336	
	Cu^2	0.036	2.18	Constant	0	14.27	Ag	0.163	
	Constant	0.099	1.7	Ag×Zn	0	6.16	Cu^2	0.321	
	Zn^2	0.105	1.66	Zn^2	0.096	1.69	Pb	0	9.11
	Cu×Pb	0.2	1.31	Cu×Pb	0.113	1.61	Pb×Zn	0	4.32
	Cu×Zn	0.236	1.21	Pb×Zn	0.14	1.49	Zn^2	0.001	3.83
	Ag×Cu	0.275	1.11	Cu×Zn	0.265	1.12	Ag×Cu	0.033	2.23

Note: The highlighted ones indicate~~s~~ the importance of Pb, Zn, and Pb×Zn predictors in the RQPM for all trenches after several steps of optimization. The order of elimination insignificant predictors is showed by p-values (α level), and t-values indicates the importance of the predictors in the RQPM.

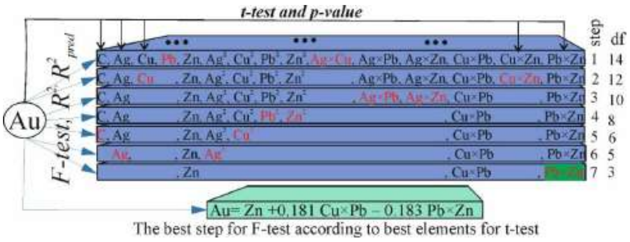

Figure 2. The differences between the t-test and F-test for optimizing model in TR2

Note: The F-test, R^2, and R^2(pred.) consider the linear relationship between Au and set of predictors which participate in modeling, while t value and p-values were calculated with the TDIST function using calculated t-values and the df for probability density function; TDIST(t, df, 2 tails)=P-value. It reveals that selecting a different predictor and model is complicated and with BE process might be facilitated by using controlling t-test and the F-tests.

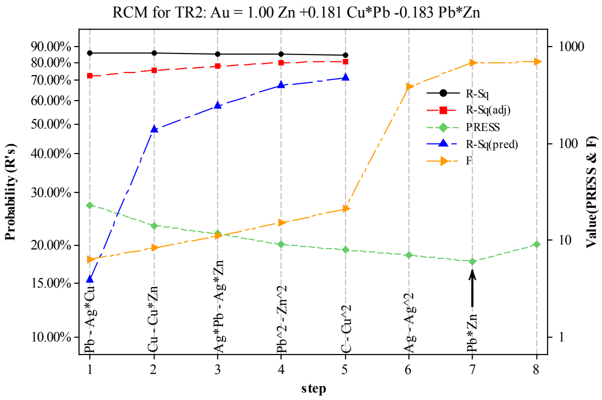

Figure 3. Optimization trend of the stepwise regression of BE using different R's (R^2, R^2[adj.], R^2[pred.]), PRESS and F-ratio criteria for TR2Discussion

Throughout this paper, the lateral geochemical dispersion pattern of Ag, Cu, Pb, and Zn are discussed considering their interactions at all trenches. We also propose an iterative model selection approach from QPM to RQPM, based on the main, quadratic terms and the interaction effects of elements. By applying interaction effects, different geochemical properties of elements have been considered using the BE procedure. Besides, the main elements and interactions are recognized in all trenches. After 8 steps of optimization and removing insignificant predictors at the TR2, R^2(pred.) increased from 15 % to more than 71 %. Accordingly, Zn and Pb×Zn were determined as the highest important element and interaction for Au modeling, respectively. This result is confirmed by the trends of other criteria (R^2, R^2[adj.], PRESS and F-ratio). The same process was applied for the other trenches (TR1, TR3, TR4, TR5, TR6) to interpret the lateral geochemical dispersion pattern of elements, respectively.

Based on the RQPM of trench TR2, it reveals that Zn, Cu×Pb and Pb×Zn were determined as the main predictors for Au (Table 4). Therefore, Zn and Pb are the most important predictors that show the same lateral dispersion (resulted from TR2 modeling) at the Glojeh deposit.

The results from Table 3 and Table 4 are clearly indicated in Table 5. The significant predictors contributing in RQPM for all trenches (Table 4) are depicted according to the t-values in the Figure 2.Accordingly,Pb and Zn are the main elements, and Pb×Zn is the main interaction which has the same geochemical dispersion pattern with Au within TR1, TR2, TR3, and TR6 (Table 5). Besides, the t-value from regular RQPM models for TR1, TR2, TR3 and TR6 indicates the strong effects of Pb and Zn. Whereas, TR4 and TR5 which are excavated in the high-grade zone contain mineralized quartz veins, veinlets and brecciated zones emphasizing that Cu and Pb are important elements for Au modeling.The most other important predictors is threshold value (the constant) that was derived from a lot of veinlets and brecciated zones at these trenches. All the step-by-step BE process of the trenches revealed that Pb and Zn accompanied with their interaction (Pb×Zn) have the same geochemical dispersion pattern and lateral variation with Au.

In order to identify Au, Ag, Cu, Pb, and Zn relationships with vein, veinlet, and brecciated zones and to better understand of their distribution in the region, preparation of a surface contour maps can aidin interpretation of results. The 2D contour maps were obtained based on trench data, a geological map, and scattered data from veins and veinlets using kriging technique. The parameters used to interpolate the map were the Gaussian for semivariogram model with output cell size (Lag size) equals 5 meters, search radius fixed in 10 meter distance and 3 is the minimum number of points were the kriging parameters used to create these maps. This method is the best linear unbiased estimator with the lowest estimation variance [28-30]. The possibility of occurrence of errors due to the lack of adequate information from the area is possible in this method to interpolation some cells. The highly Au concentrated samples have spread between TR2 and TR6, where the highest anomalous samples appears around TR4 and TR5 (Figure 4A). Also, ore-bearing major veins and veinlets trend are nearly east-westward (see Figure 1), while it was evident in the kriging surface variation of Au concentration (Figure 4A). The observed surface anomalies for Au show similar trend and largely overlap on Pb and Zn concentrated samples (Figure 4A, 4B, and 4C).

Table 5. The results of BE to recognize significant and insignificant predictors for trench

trench	threshold value	significant elements in RQPM	significant interactions in RQPM	insignificant predictors
TR1, Tr2, TR3 and TR6	-	Pb, Zn	Pb×Zn	Ag, C, Ag×Cu
TR4 and TR5	ok	Cu, Pb	Ag×Zn, Pb×Zn	Ag^2, Pb^2

Zn and Pb show the same variation of the concentration at deeper zones and Zn is highly enriched in superficial horizons [31]. On the other hand, these finding can be approved using BE modeling results. Mehrabi, Siani, Goldfarb, Azizi, Ganerod and Marsh [17]indicated that Au is certainly mineralized in the epithermal brecciated zones in late stages of magmatic fluids and afterward directly precipitated in associated meteoric water, whereas Cu is precipitated in early and middle stages and magmatic fluids have a greater role in mineralization. Therefore, the Glojeh deposit may be associated with a porphyry mineralization at depth.In order to the evaluation of the Au concentration by optimization process of the quadratic polynomial model, Cu, Pb and Zn are well separated laterally.

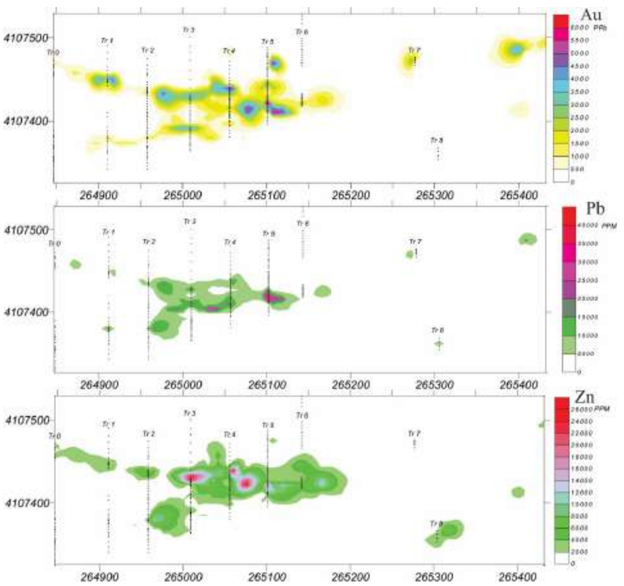

Figure 4. The 2D Glojeh surface contour map of Au (A); Pb (B); and Zn (C)

5. Conclusion

By constructing interaction effects of elements the relationship between variables could be distinguished, too much better. Where in environmental and mining science (certainly in mineralization) all the elements acts related and they must considered simultaneously, hence application of elemental interactions could ease to accurate modeling. Accordingly, model reduction process is handled until the main predictors recognized. This method could applied in different multivariable studies. In the presented study it was conducted to recognize the horizontal relationship (lateral dispersion or elemental zoning) between variables, statistically and spatially, determine an indicator model and decrease the cost of Au analysis. Iterative BE based on RA and ANOVA for 6 trenches (782 meter) indicates that optimized model consisting of interaction effects can reveal the lateral dispersion pattern of predictors. All the RQPMs were confirmed by the trends of R^2, R^2(-adj.), R^2(pred.) and F-ratio criteria. By investigating and modeling trenches, it was found that Pb and Zn are the main elements and Pb×Zn is an interacted predictor to determine linear productivity or lateral dispersion of Au. But in TR4 and TR5 trenches which located on veins/veinlets, brecciated zones, and silicic alteration, the threshold is significant parameter.

The present study indicates that by incorporation of interaction effects and application of regression analysis and the BE procedure method could easily explain the dispersion and variation of Au and associated elements. Some of the results from the BE based on iterative stepwise re-

DOI: https://doi.org/10.30564/jmmr.v2i1.1001

gression revealed that lateral dispersion of elements were overlapped and confirmed with 2D surface contour maps using a kriging technique. A distinct vertical zonation which appeared by a transition zone in depth may indicate a porphyry deposits at the depth. In addition, lateral geochemical dispersion pattern for Au determined using Zn>Cu×Pb>Pb×Zn predictors.

Acknowledgments

The authors also are hugely thankful to shima allahyari for their encouragement and valuable help.

References

[1] Raudenbush, S.W. and Liu, X.-F.. “Effects of study duration, frequency of observation, and sample size on power in studies of group differences in polynomial change”. Psychological methods 2001, 6, 387.

[2] Diggle, P.. “Analysis of Longitudinal Data, Edited by Diggle PJ, Heagerty P, Liang KY, Zeger SL”. Oxford, Oxford University Press, 2002.

[3] Leon, A.C. and Heo, M..“Sample sizes required to detect interactions between two binary fixed-effects in a mixed-effects linear regression model”. Computational statistics & data analysis, 2009, 53: 603-608.

[4] Graham, M.W. and Miller, D.J.. “Unsupervised learning of parsimonious mixtures on large spaces with integrated feature and component selection”. IEEE Transactions on Signal Processing, 2006, 54: 1289-1303.

[5] Samal, A.R., et al..“Backward elimination procedure for a predictive model of gold concentration”. Journal of Geochemical Exploration, 2008, 97: 69-82.

[6] Garson, G.. “Multiple regression (statistical associates blue book series)”. Asheboro, NC: Statistical Associates Publishers, 2012.

[7] Mohammadi, R., et al.. “Extraction optimization of pepsin-soluble collagen from eggshell membrane by response surface methodology (RSM)”. Food chemistry, 2016, 190: 186-193.

[8] Yadav, V., et al.. “A backward elimination discrete optimization algorithm for model selection in spatio-temporal regression models”. Environmental modelling & software, 2013, 42: 88-98.

[9] Singh, J., et al.. “Study of sruface roughness for discontinuous ultrasonic vibration assisted electric discharge machining using RSM”. International Journal of Research in Engineering and Technology, 2013, 2: 727-737.

[10] Vaske, J.J.. “Communicating judgments about practical significance: Effect size, confidence intervals and odds ratios”. Human Dimensions of Wildlife, 2002, 7: 287-300.

[11] Eggenhuisen, J.T., et al.. “Small-scale spatial variability in turbidity-current flow controlled by roughness resulting from substrate erosion: field evidence for a feedback mechanism”. Journal of Sedimentary Research, 2010, 80: 129-136.

[12] Mousavi, J. and Parvini, M.. “A sensitivity analysis of parameters affecting the hydrogen release and dispersion using ANOVA method”. International Journal of Hydrogen Energy, 2016, 41: 5188-5201.

[13] Mehrabi, B., et al.. “The genesis of the epithermal gold mineralization at North Glojeh veins, NW Iran”. IJSAR , 2014, 15: 479-497.

[14] Ghorbani, M.. The economic geology of Iran: mineral deposits and natural resources. Springer Science & Business Media, 2013.

[15] Alavi, M.. “Tectonostratigraphic synthesis and structural style of the Alborz mountain system in northern Iran”. Journal of Geodynamics, 1996, 21: 1-33.

[16] Bahajroy, M. and Taki, S.. “Study of the mineralization potential of the intrusives around Valis (Tarom-Iran)”. Earth Sciences Research Journal, 2014, 18: 123-129.

[17] Mehrabi, B., et al.. “Mineral assemblages, fluid evolution, and genesis of polymetallic epithermal veins, Glojeh district, NW Iran”. Ore Geology Reviews, 2016, 78: 41-57.

[18] Barnes, H.L.. Geochemistry of hydrothermal ore deposits. John Wiley & Sons, 1997.

[19] Cheng, Q.. “Mapping singularities with stream sediment geochemical data for prediction of undiscovered mineral deposits in Gejiu, Yunnan Province, China”. Ore Geology Reviews, 2007, 32: 314-324.

[20] Braams, B.R., et al.. “Longitudinal changes in adolescent risk-taking: a comprehensive study of neural responses to rewards, pubertal development, and risk-taking behavior”. The Journal of Neuroscience, 2015, 35: 7226-7238.

[21] Darabi-Golestan, F. and Hezarkhani, A.. “Quadratic investigation of geochemical distribution by backward elimination approach at Glojeh epithermal Au (Ag)-polymetallic mineralization, NW Iran”. Journal of Central South University, 2018, 25: 342-356.

[22] Preacher, K.J., et al.. “Computational tools for probing interactions in multiple linear regression, multilevel modeling, and latent curve analysis”. Journal of educational and behavioral statistics, 2006, 31: 437-448.

[23] Ali, K., et al.. “Application of empirical and semi-analytical algorithms to MERIS data for estimating chlorophyll a in Case 2 waters of Lake Erie”. Environmental Earth Sciences, 2014, 71: 4209-4220.

DOI: https://doi.org/10.30564/jmmr.v2i1.1001

[24] Coruh, S. and Elevli, S.. "Optimization of malachite green dye removal by sepiolite clay using a central composite design". Global NEST Journal, 2014, 16: 339-347.

[25] Nelson, J.B.. "A Robust Function to Return the Cumulative Density of Non-Central F Distributions in Microsoft Office Excel". Psicologica: International Journal of Methodology and Experimental Psychology, 2016, 37: 61-83.

[26] Darabi-Golestan, F. and Hezarkhani, A.. "Applied statistical functions and multivariate analysis of geochemical compositional data to evaluate mineralization in Glojeh polymetallic deposit, NW Iran". Frontiers of Earth Science, 2019, 13: 229-246.

[27] Darabi-Golestan, F. and Hezarkhani, A.. "Discrimination geochemical interaction effects on mineralization at the polymetallic Glojeh deposit, NW Iran by interative backward quadratic modeling". Acta Geochimica, 2019.

[28] Wackernagel, H.. " Kriging Weights". In Multivariate Geostatistics, 2003: 89-95, Springer.

[29] Samal, A.R., et al.. "Modelling spatial anisotropy of gold concentration data using GIS-based interpolated maps and variogram analysis: Implications for structural control of mineralization". Journal of earth system science, 2011, 120: 583-593.

[30] Asghari, O., et al.. "The comparison between sequential gaussian simulation (SGS) of Choghart ore deposit and geostatistical estimation through ordinary kriging". Australian Journal of Basic and Applied Sciences, 2009, 3: 330-341.

[31] Darabi-Golestan, F. and Hezarkhani, A.. "Evaluation of elemental mineralization rank using fractal and multivariate techniques and improving the performance by log-ratio transformation". Journal of Geochemical Exploration, 2018, 189: 11-24.

DOI: https://doi.org/10.30564/jmmr.v2i1.1001

Author Guidelines

This document provides some guidelines to authors for submission in order to work towards a seamless submission process. While complete adherence to the following guidelines is not enforced, authors should note that following through with the guidelines will be helpful in expediting the copyediting and proofreading processes, and allow for improved readability during the review process.

Ⅰ. Format

- Program: Microsoft Word (preferred)
- Font: Times New Roman
- Size: 12
- Style: Normal
- Paragraph: Justified
- Required Documents

Ⅱ. Cover Letter

All articles should include a cover letter as a separate document.

The cover letter should include:

- Names and affiliation of author(s)

The corresponding author should be identified.

Eg. Department, University, Province/City/State, Postal Code, Country

- A brief description of the novelty and importance of the findings detailed in the paper

Declaration

v Conflict of Interest

Examples of conflicts of interest include (but are not limited to):

- Research grants
- Honoria
- Employment or consultation
- Project sponsors
- Author’s position on advisory boards or board of directors/management relationships
- Multiple affiliation
- Other financial relationships/support
- Informed Consent

This section confirms that written consent was obtained from all participants prior to the study.

- Ethical Approval

Eg. The paper received the ethical approval of XXX Ethics Committee.

- Trial Registration

Eg. Name of Trial Registry: Trial Registration Number

- Contributorship

The role(s) that each author undertook should be reflected in this section. This section affirms that each credited author has had a significant contribution to the article.

1. Main Manuscript
2. Reference List
3. Supplementary Data/Information

Supplementary figures, small tables, text etc.

As supplementary data/information is not copyedited/proofread, kindly ensure that the section is free from errors, and is presented clearly.

Ⅲ. Abstract

A general introduction to the research topic of the paper should be provided, along with a brief summary of its main results and implications. Kindly ensure the abstract is self-contained and remains readable to a wider audience. The abstract should also be kept to a maximum of 200 words.

Authors should also include 5-8 keywords after the abstract, separated by a semi-colon, avoiding the words already used in the title of the article.

Abstract and keywords should be reflected as font size 14.

Ⅳ. Title

The title should not exceed 50 words. Authors are encouraged to keep their titles succinct and relevant.

Titles should be reflected as font size 26, and in bold type.

Ⅳ. Section Headings

Section headings, sub-headings, and sub-subheadings should be differentiated by font size.

Section Headings: Font size 22, bold type

Sub-Headings: Font size 16, bold type

Sub-Subheadings: Font size 14, bold type

Main Manuscript Outline

Ⅴ. Introduction

The introduction should highlight the significance of the research conducted, in particular, in relation to current state of research in the field. A clear research objective should be conveyed within a single sentence.

Ⅵ. Methodology/Methods

In this section, the methods used to obtain the results in the paper should be clearly elucidated. This allows readers to be able to replicate the study in the future. Authors should ensure that any references made to other research or experiments should be clearly cited.

Ⅶ. Results

In this section, the results of experiments conducted should be detailed. The results should not be discussed at length in this section. Alternatively, Results and Discussion can also be combined to a single section.

Ⅷ. Discussion

In this section, the results of the experiments conducted can be discussed in detail. Authors should discuss the direct and indirect implications of their findings, and also discuss if the results obtain reflect the current state of research in the field. Applications for the research should be discussed in this section. Suggestions for future research can also be discussed in this section.

Ⅸ. Conclusion

This section offers closure for the paper. An effective conclusion will need to sum up the principal findings of the papers, and its implications for further research.

Ⅹ. References

References should be included as a separate page from the main manuscript. For parts of the manuscript that have referenced a particular source, a superscript (ie. [x]) should be included next to the referenced text.
[x] refers to the allocated number of the source under the Reference List (eg. [1], [2], [3])
In the References section, the corresponding source should be referenced as:
[x] Author(s). Article Title [Publication Type]. Journal Name, Vol. No., Issue No.: Page numbers. (DOI number)

Ⅺ. Glossary of Publication Type

J = Journal/Magazine

M = Monograph/Book

C = (Article) Collection

D = Dissertation/Thesis

P = Patent

S = Standards

N = Newspapers

R = Reports

Kindly note that the order of appearance of the referenced source should follow its order of appearance in the main manuscript.
Graphs, Figures, Tables, and Equations
Graphs, figures and tables should be labelled closely below it and aligned to the center. Each data presentation type should be labelled as Graph, Figure, or Table, and its sequence should be in running order, separate from each other.
Equations should be aligned to the left, and numbered with in running order with its number in parenthesis (aligned right).

Ⅻ. Others

Conflicts of interest, acknowledgements, and publication ethics should also be declared in the final version of the manuscript. Instructions have been provided as its counterpart under Cover Letter.

BILINGUAL
PUBLISHING CO.
Pioneer of Global Academics Since 1984

Journal of Metallic Material Research

Aims and Scope

Journal of Metallic Material Research is a peer-reviewed, open-access journal dedicated to the research of metallic materials. As a critical component of the human civilization, metal has been infused into many aspects of our lives. The journal is focused on innovations in the research of metallic materials.

The scope of the Journal of Metallic Material Research includes, but is not limited to:

- Properties of metallic materials (Physical/Mechanical/Electrical/Chemical)
- Functions of metallic materials
- Applications of metallic materials
- Alloys
- Recycling

Bilingual Publishing Co. (BPC)

Tel:+65 65881289

E-mail:contact@bilpublishing.com

Website:www.bilpublishing.com

About the Publisher

Bilingual Publishing Co(BPC) is an international publisher of online, open access and scholarly peer-reviewed journals covering a wide range of academic disciplines including science, technology, medicine, engineering,education and social science. Reflecting the latest research from a broad sweep of subjects, our content is accessible worldwide – both in print and online.

BPC aims to provide an analytics as well as platform for information exchange and discussion that help organizations and professionals in advancing society for the betterment of mankind. SP hopes to be indexed by well-known databases in order to expand its reach to the science community, and eventually grow to be a reputable publisher recognized by scholars and researchers around the world.

BPC adopts the Open Journal Systems, see on http://ojs.s-p.sg

Database Inclusion

National Library, Singapore

Asia & Pacific area Science Citation Index

China National Knowledge Infrastructure

Creative Commons

Google Scholar

Crossref

J-Gate

My Science Work

National Library of Singapore

NLB manages the National Library, 26 Public Libraries and the National Archives.

NLB promotes reading, learning and information literacy by providing a trusted, accessible and globally-connected library and information service through the National Library and a comprehensive network of Public Libraries. By forging strategic partnerships to cultivate knowledge sharing, the libraries also encourage appreciation and awareness of Singapore's history through their wide range of programmes and collection on Singapore and regional content. The National Archives of Singapore oversees the collection, preservation and management of public and private archival records, including government files, private memoirs, maps, photographs, oral history interviews and audio-visual materials.

Established on 1 September 1995 as a statutory board, NLB is an agency under the Ministry of Communications and Information (MCI).

Bilingual Publishing Co. is a company registered in Singapore in 1984, whose office is at 12 Eu Tong Sen Street, #08-169, Singapore 059819, enjoying a high reputation in Southeast Asian countries, even around the world.

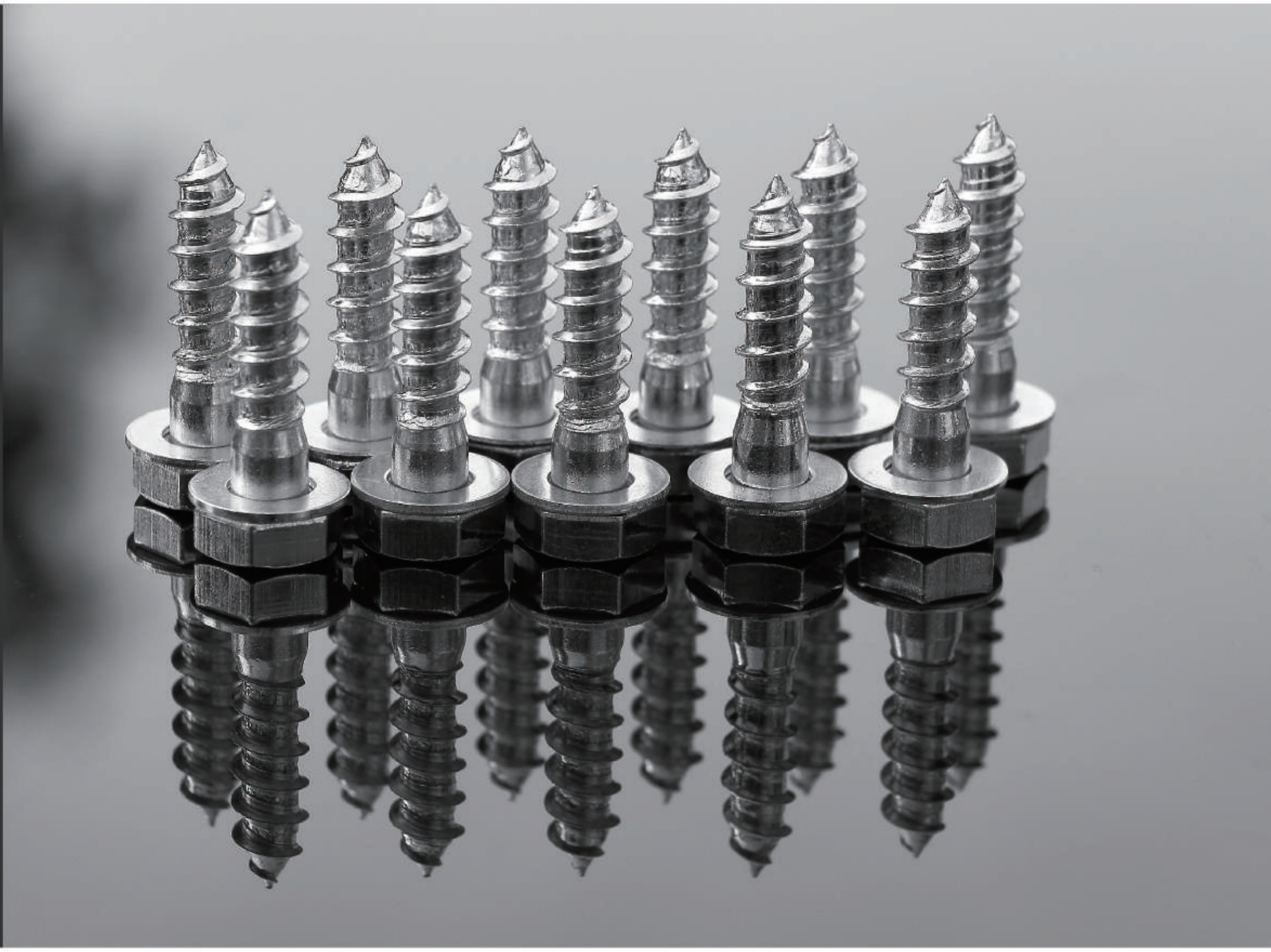

Tel:+65 65881289
E-mail:contact@bilpublishing.com
Website:www.bilpublishing.com

BILINGUAL
PUBLISHING CO.
Pioneer of Global Academics Since 1984

ISSN 2630-5135
01
9 772630 513199